POLITECNICO DI TORINO
Repository ISTITUZIONALE

Real-time simulation of torque and nitrogen oxide emissions in an 11.0 L heavy-duty diesel engine for model-based combustion control

Original
Real-time simulation of torque and nitrogen oxide emissions in an 11.0 L heavy-duty diesel engine for model-based combustion control / Finesso, Roberto; Hardy, Gilles; Mancarella, Alessandro; Marello, Omar; Mittica, Antonio; Spessa, Ezio. - In: ENERGIES. - ISSN 1996-1073. - STAMPA. - 12:3(2019), p. 460. [10.3390/en12030460]

Availability:
This version is available at: 11583/2725437 since: 2021-04-01T10:59:52Z

Publisher:
MDPI AG

Published
DOI:10.3390/en12030460

Terms of use:

This article is made available under terms and conditions as specified in the corresponding bibliographic description in the repository

Publisher copyright

(Article begins on next page)

12 October 2024

energies

MDPI

Article

Real-Time Simulation of Torque and Nitrogen Oxide Emissions in an 11.0 L Heavy-Duty Diesel Engine for Model-Based Combustion Control

Roberto Finesso [1,*], Gilles Hardy [2], Alessandro Mancarella [1], Omar Marello [1], Antonio Mittica [1] and Ezio Spessa [1]

1 Department of Energy, Politecnico di Torino, Corso Duca degli Abruzzi 24, 10129 Torino, Italy; alessandro.mancarella@polito.it (A.M.); omar.marello@polito.it (O.M.); antonio.mittica@polito.it (A.M.); ezio.spessa@polito.it (E.S.)

2 FPT Motorenforschung AG, Schlossgasse 2, 9320 Arbon, Switzerland; gilles.hardy@cnhind.com

* Correspondence: roberto.finesso@polito.it; Tel.: +39-011-090-4493

Received: 13 December 2018; Accepted: 30 January 2019; Published: 31 January 2019

Abstract: A real-time combustion model was assessed and applied to simulate BMEP (Brake Mean Effective Pressure) and NO_x (Nitrogen Oxide) emissions in an 11.0 L FPT Cursor 11 diesel engine for heavy-duty applications. The activity was carried out in the frame of the IMPERIUM H2020 EU Project. The developed model was used as a starting base to derive a model-based combustion controller, which is able to control indicated mean effective pressure and NO_x emissions by acting on the injected fuel quantity and main injection timing. The combustion model was tested and assessed at steady-state conditions and in transient operation over several load ramps. The average root mean square error of the model is of the order of 110 ppm for the NO_x simulation and of 0.3 bar for the BMEP simulation Moreover, a statistical robustness analysis was performed on the basis of the expected input parameter deviations, and a calibration sensitivity analysis was carried out, which showed that the accuracy is almost unaffected when reducing the calibration dataset by about 80%. The model was also tested on a rapid prototyping device and it was verified that it features real-time capability, since the computational time is of the order of 300–400 µs. Finally, the basic functionality of the model-based combustion controller was tested offline at steady-state conditions.

Keywords: model-based; control; heavy-duty; diesel engine; NOx emissions; BMEP

1. Introduction

1.1. Background

The need to comply with the more and more stringent regulations in terms of CO_2 and pollutant emissions is pushing the automotive industry to develop innovative technologies. Recent trends which may produce the highest benefits include engine downsizing [1], alternative fuels (such as Compressed Natural Gas (CNG) and biofuels) [2], innovative combustion concepts such as Homogeneous Charge Compression Ignition (HCCI) and Premixed Charge Compression Ignition (PCCI) [3], advanced high-pressure common rail systems [4,5], innovative combustion controls [6–8], innovative after-treatment system (ATS) technologies [9], kinetic and thermal energy recovery [10], vehicle road load reduction [11], powertrain electrification [12], and vehicle connectivity (V2X technologies) [13]. In particular, in ref. [1] the authors describe the potential benefits of the electrically-assisted turbocharger with VGT to enable heavy-duty diesel engine downsizing. The study reported in ref. [2] pointed out the benefits of the use of biodiesel on the Diesel Particulate Filter (DPF) particulate emissions. In ref. [3] an experimental study is reported, which shows the potential of PCCI

combustion in dramatically reducing engine-out nitrogen oxides and soot emissions in a 3.0 L diesel engine, with the possibility of reviewing the after treatment system. In ref. [4] an innovative common rail system with reduced accumulator is compared with a standard one, while in ref. [5] the same authors propose several guidelines for the reduction of leakage in injection systems. In refs. [6,7] the authors propose a controller of MFB50 and of BMEP/NO_x emissions, respectively, for a 3.0 L diesel engine, while in ref. [8] a neural network-based approach is proposed for the control of torque and MFB50 for a 1.6 L diesel engine. The paper proposed in ref. [9] shows the main advancements in diesel and spark ignition engine emissions, including the impact of the after-treatment devices. In ref. [10], the authors investigate the available energy of the waste heat from a high boosted 6-cylinder heavy duty diesel engine which is equipped with high and low pressure loop Exhaust Gas recirculation (EGR) system, showing that the estimated improvement in fuel consumption by the Rankine combined cycle is about 2.7% in a single-stage turbocharged system and 2.9% in a 2-stage turbocharged system. In ref. [11] the authors compare reference and lightweight design solutions in terms of global warming potential. The study reported in ref. [12] presents a tool for the optimal design of hybrid vehicles equipped with diesel engines, and the consequent benefits in terms of costs and CO_2 emission reduction. Finally, in ref. [13] a cooperative adaptive cruise control system that combines precise positioning at the lane level and V2X communications was developed, with the aim of reducing CO_2 emissions in dense traffic conditions.

Among these technologies, model-based combustion controls seem to have a good potential in order to achieve both fuel consumption and pollutant emission reductions, compared to the traditional map-based approach. This has been made possible by the recent advances in the computational performance of engine control units (ECUs), which are now capable of executing more and more complex model-based algorithms in real-time. The advantages of model-based controllers against conventional map-based ones are due to several reasons. For example, a model-based approach allows an onboard optimization of the combustion process to be realized, by adjusting the main engine control variables in real-time, in order to achieve desired targets of performance or pollutant emission metrics. Moreover, model-based combustion controllers can be coupled with additional model-based control modules which could be available in the ECU (such as ATS management), in order to allow higher engine-out pollutant levels when the ATS efficiency is high (with benefits in terms of fuel consumption) and lower engine-out pollutant levels when the ATS efficiency is low. It should also be considered that model-based combustion controllers may be integrated with the emerging V2V and V2I technologies. For example, if the road characteristic and traffic conditions are known in advance (on the basis of an eHorizon system), the vehicle energy management supervisor may request the engine combustion controller to realize specific instantaneous targets of torque and/or engine-out pollutant emissions, in order to globally optimize the performance of the vehicle in the future time frame.

In addition to the previous aspects, it should be noted that model-based combustion controllers are advantageous, compared with traditional map-based controllers, also in terms of calibration effort, especially for that which concerns diesel engines. It should in fact be considered that modern diesel engines are characterized by a very high degree of complexity, and are managed by a large number of control parameters, which are defined by maps. These maps require a high calibration effort, with related consequences in terms of needed time and costs. Moreover, traditional engine maps need to be properly calibrated in order to take the variability of the environmental conditions (temperature, pressure, humidity etc.) into account, while a model-based approach is in general more robust with respect to these kinds of effects.

The previous considerations justify why the interest in the development of model-based combustion controls for ICEs (Internal Combustion Engines) and, more specifically, for diesel engines, has increased in recent years.

With reference to diesel technology, although the current social and political attitude towards this kind of technology is negative, it should be pointed out that recent innovations have allowed a dramatic reduction of NO_x emissions (far less than European standards after 2020, see ref. [14]),

also exploiting artificial intelligence technology. Moreover, diesel technology is expected to remain the best solution for light-duty and heavy-duty long haul applications, in which it offers incontestable advantages in terms of both fuel consumption and fuel costs. These advantages may be amplified by means of powertrain electrification.

Given the previous background, a real-time combustion model was developed in this study, capable of predicting BMEP (Brake Mean Effective Pressure) and NO_x emissions in an 11 L FPT Cursor 11 heavy-duty diesel engine. The model is intended to be used for the development of a model-based combustion controller to be implemented in the engine, within the IMPERIUM (IMplementation of Powertrain Control for Economic and Clean Real driving emIssion and fuel ConsUMption") EU H2020 collaborative research project.

This project started in 2016, and is currently ongoing. Its main objective is to achieve fuel consumption and urea reduction of up to 20% for long haulage heavy-duty trucks, while keeping the vehicle within the legal limits for pollutant emissions [15]. The consortium includes three major manufacturers of heavy duty trucks (DAF Trucks N.V, IVECO S.p.A. and Volvo Technology AB), eight major high end and large component and engineering service suppliers (FPT Motorenforschung AG, AVL List GmbH, Ricardo UK Ltd., Continental Automotive GmbH, FEV GmbH, Robert Bosch GmbH, and Honeywell SPOL. S.R.O), as well as six research and service centers specializing in simulations (Chalmers University, Politecnico di Torino, Politecnico di Milano, CTU Prague, RWTH Aachen University, Technical University Eindhoven).

The consortium will realize three heavy-duty demonstrators, in which the fuel consumption and urea reduction benefits will be achieved through several technologies, including the use of an energy management supervisor, dynamic e-horizon system, model-based engine control, waste heat recovery, micro-hybrid and smart auxiliaries.

1.2. State of the Art in Low-Throughput Combustion Modeling for Model-Based Combustion Control

In general, low computationally demanding simulation models are required for the development of model-based combustion controllers, due to the fact that the ECU must be capable of running these controllers in real time, often on a cycle-by-cycle basis.

Therefore, multidimensional or one-dimensional approaches are not suitable for this purpose.

The best candidates for the development of model-based combustion controllers are mean-value zero-dimensional models and artificial intelligent systems [7].

Mean-value zero-dimensional models are capable of simulating the combustion and/or pollutant formation processes on the basis of a physical approach, and require at the same time a low computational effort compared to 3D-CFD or 1D-CFD approaches. Some examples are provided in refs. [16–20]. In particular, in ref. [16] the potential of mean-value models, especially of the filling and emptying approach, is discussed for the simulation of transient conditions. In ref. [17], the authors propose a real-time mean value engine model, which is capable of simulating the in-cylinder pressure and NOx emissions. The model was tested at steady-state and transient conditions and showed a good accuracy over New European Driving Cycle (NEDC) and Worldwide harmonized Light-duty Test Procedure (WLTP) missions. In ref. [18] a simple, physics-based model for the NO_x emissions of diesel engines was developed and validated using data from three different engines, showing an error during transients of 2.5% in average. In ref. [19], the previous model is embedded in a mean-value model for the air path. In ref. [20] a real time NO_x calculation model is proposed, which takes into account fuel injection, ignition delay, premixed heat release rate and diffusion combustion heat release rate.

These models usually show very good performance at steady-state operation and an acceptable accuracy in mildly transient conditions. In general, they do not require a high calibration effort, due to their physics-based nature, and are quite robust outside the calibration range.

Artificial intelligence systems include different methodologies, such as, support vector machine (SVM), fuzzy logics, and artificial neural networks (ANNs). These methods belong to the black-box category, and are often used for model-based control purposes since they require a low computational

effort. They are capable of capturing the non-linear behaviors of complex systems, without the need of modeling the physics of the process to be simulated. The main drawback of these types of models is that they require, in general, a high number of experimental tests for robust training, and tend to lose accuracy when extrapolating outside the calibration range. Moreover, they can be subject to overfitting. Some examples are reported in refs. [21–25]. In particular, in ref. [21] an ANN-based model was developed and applied to predict the variation of energy efficiency, exergy efficiency and exhaust temperature based on biodiesel type and engine load. In ref. [22] an ANN-based model was implemented and used to predict combustion product composition and gas thermodynamic properties. In ref. [23], a recurrent non-linear autoregressive with exogenous input (NARX) neural network is proposed, for reconstructing cylinder pressure in multi-cylinder IC engines using measured crank kinematics. The study proposed in ref. [24] illustrates NO_x and smoke emission models based on an artificial neural network approach with Multi-Layer Perceptron (MLP) architectures. The results show that both models are capable of capturing the highly nonlinear engine-out emissions high accuracy and strong generalization performance over NEDC and WLTP missions. Finally, in ref. [25] the authors propose hierarchical models, namely "neuro-fuzzy model trees", to predict transient particulate mass and NO_x.

In this paper, a low-throughput mean-value zero dimensional model was considered, due to its physical consistency and low requirements in terms of calibration effort.

1.3. Contribution of the Present Study

The main contributions of this study are summarized hereafter.

1. A real-time predictive combustion model, that was previously developed by the authors for small and medium displacement engines [6–8,17], was assessed and applied to simulate BMEP and NO_x emissions in a 11.0 L FPT Cursor 11 heavy-duty diesel engine. Several improvements and adaptations were implemented in the previous model version, in order to optimize its performance for a large displacement engine.
2. The model was extensively validated over about 2200 experimental tests, which include engine maps with and without pilot and EGR rate, sweep tests of injection pressure and injection timing, as well as sweep tests of EGR and VGT rack position. An extended validation of this type has not been addressed in the past, with reference to previous applications.
3. The model was also validated in transient operation, considering load ramps at different engine speeds.
4. A model robustness analysis to input parameters was carried out, in order to analyze the effect of the uncertainty of the main model input parameter on the accuracy of the main model outcomes.
5. A calibration sensitivity analysis was carried out, in order to investigate the impact of the number and type of experimental tests used for model calibration on the accuracy.
6. An analysis of the computational time that is required by the model, when it is run on an ETAS ES910 rapid prototyping device, was carried out. This is a preliminary step in order to check the real-time capability of the proposed approach and its suitability for the development of a model-based controller.
7. The model was inverted in order to derive a model based combustion controller, which receives targets of IMEP (Indicated Mean Effective Pressure) and engine-out NO_x emissions, and sets the injected fuel quantity and main injection timing in order to achieve the desired targets. This controller was developed starting from a previous version [7]. However, several features were added in order to improve its performance and robustness in view of the implementation on a real engine. A preliminary assessment of the controller was carried out at steady-state conditions.

2. Experimental Setup and Engine Conditions

The experimental tests were measured for a FPT C11 11.0 L diesel engine. The main engine specifications are reported in Table 1.

Table 1. Main technical specifications of the FPT Cursor 11 engine.

Engine Specifications	
Engine type	FPT Cursor 11 diesel engine
Number of cylinders	6
Displacement	11.1 dm^3
Bore × stroke	128 mm × 144 mm
Conrod length	228 mm
Compression ratio	20
Valves per cylinder	4
Turbocharger	VGT type
Fuel injection system	High pressure Common Rail

The engine scheme, including the main measurement sensors, is shown in Figure 1. A short-route EGR system equipped with a cooler is installed on the engine. The EGR valve is installed upstream from the EGR cooler. A flap is present in the exhaust pipe downstream of the turbine, in order to control the temperature of the exhaust gas flowing to the after-treatment system and to increase the EGR rate if necessary. The ATS system includes a Diesel Oxidation Catalyst (DOC), a DPF, an Selective Catalytic Reduction (SCR) and a Clean-Up Catalyst (CUC).

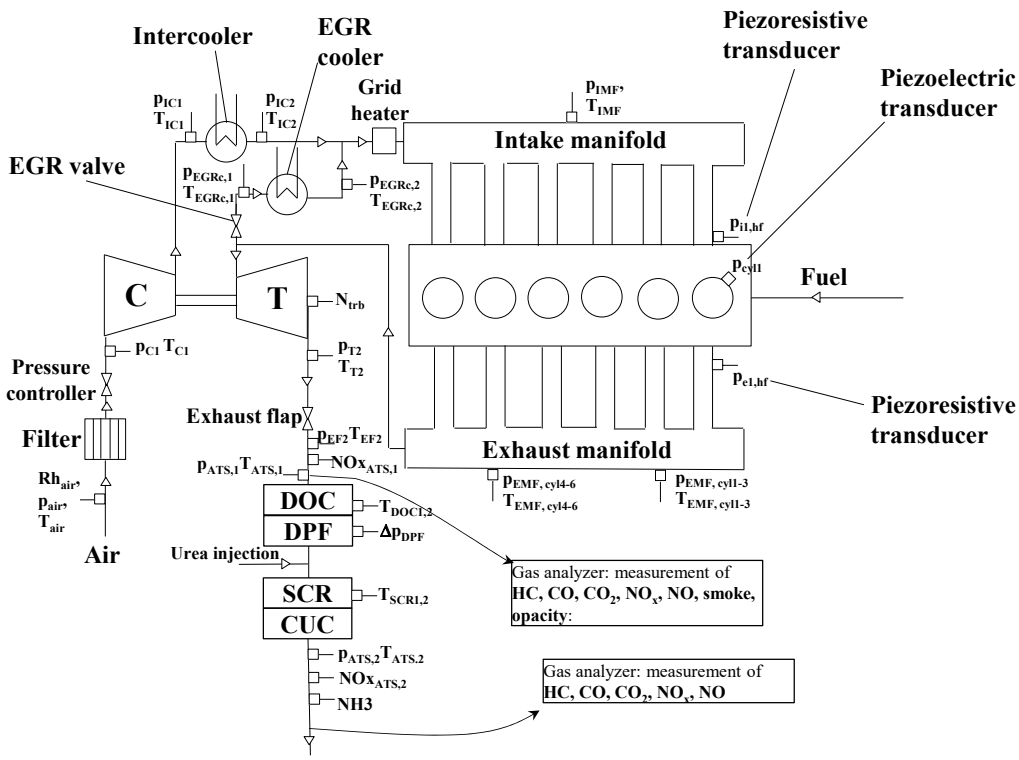

Figure 1. Scheme of the FPT Cursor 11diesel engine installed on the highly dynamic test bench in Arbon. The main measurement locations are also indicated.

The test engine was instrumented with standard K-type thermocouples and piezo-resistive pressure transducers in order to acquire temperature and pressure at several locations, such as upstream from the compressor (p_{C1}, T_{C1}), upstream and downstream from the intercooler (p_{IC1}, T_{IC1}, p_{IC2}, T_{IC2}), upstream and downstream from the EGR cooler ($p_{EGRc,1}$, $T_{EGRc,1}$, $p_{EGRc,2}$, $T_{EGRc,2}$), in the

intake manifold (p_{IMF}, T_{IMF}), in the exhaust manifold ($p_{EMF,cyl1-3}$, $T_{EMF,cyl1-3}$, $p_{EMF,cyl4-6}$, $T_{EMF,cyl4-6}$), downstream from the turbine (p_{T2}, T_{T2}), downstream from the exhaust flap (p_{EF2}, T_{EF2}), upstream and downstream from the ATS system ($p_{ATS,1}$, $T_{ATS,1}$, $p_{ATS,2}$, $T_{ATS,2}$). The temperature was also measured upstream and downstream from DOC ($T_{DOC,1}$, $T_{DOC,2}$) and SCR ($T_{SCR,1}$, $T_{SCR,2}$). Moreover, for the ATS management, the ECU received information concerning the pressure differential across the DPF (Δp_{DPF}), the NOx concentration upstream and downstream from ATS ($NOx_{ATS,1}$, $NOx_{ATS,2}$), and the NH_3 concentration downstream from the SCR (NH3). The NOx concentrations upstream and downstream from the ATS system were obtained from two NOx sensors, characterized by an error of the order of 5–10%.

A Kistler 6045A high-frequency piezo-electric transducer (p_{cyl1}) was placed inside cylinder 1, in order to acquire the in-cylinder pressure time-history on a crank basis. The in-cylinder pressure traces were pegged on the basis of the intake absolute pressure that was measured by means of a high-frequency Keller M510 piezo-resistive transducer, located in front of cylinder 1 ($p_{i1,hf}$). On the exhaust side, a high-frequency cooled Kistler 4075A10 piezo-resistive transducer was also installed ($p_{e1,hf}$) to measure the absolute exhaust pressure.

The tests were carried out at a dynamic test rig at the FPT Motorenforschung in Arbon. Figure 2 shows a scheme of the test bench.

The test bench is equipped with a Schenck dynamometer (maximum power/torque/speed: 570 kW/3200 Nm/4000 rpm) and a PLU 401/121 fuel meter (measurement range: 0.35–150 L/h).

The raw engine-out gaseous emissions were measured by means of a Pierburg AMA4000 gas analyzer.

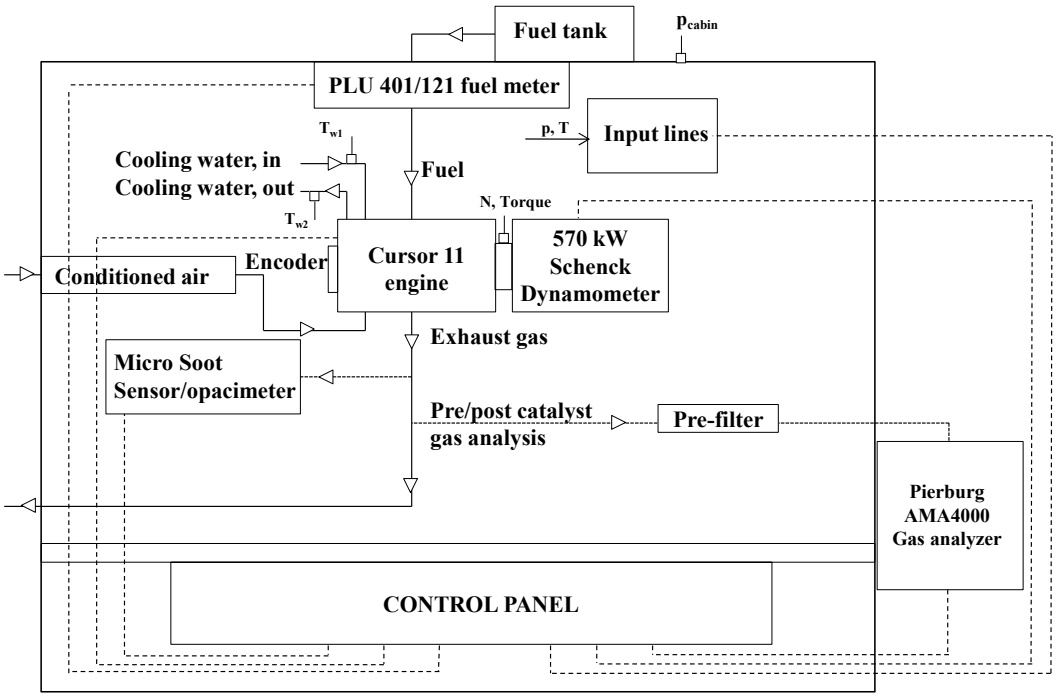

Figure 2. Scheme of the test bench.

The developed combustion model was tested on an ETAS ES910 rapid prototyping device, in order to check its real-time capability. The device specifications are shown in Table 2.

Finally, Table 3 reports a summary of the accuracy of the main test bench sensors that were used to derive the experimental variables used for the model assessment.

Table 2. Main specifications of the ETAS ES910 device.

ETAS ES910 Device	
Main processor	Freescale PowerQUICC™ III MPC8548 with 800 MHz clock Double precision floating point unit
Memory	512 MByte DDR2-RAM (400 MHz clock) 64 MByte Flash 128 kByte NVRAM

Table 3. Accuracy of the main test bench sensors.

Measurement Device	Accuracy
Encoder	Resolution: 0.1° CA
Fuel meter	Error < ±0.1% of read value
Torque meter	Error < ±0.95 Nm
In-cylinder pressure sensor	Linearity error: < ±0.4% of Full Span (250 bar)
NO_x CLD device in the gas analyzer	Error < ±5% of read value when NO/NO_x = 90% Error < ±10% of read value when NO_2/NO_x = 90%
O_2 POD device in the gas analyzer	Error < ±5% of read value

Experimental Activity

The experimental tests which were considered in this paper for model assessment and validation were carried out at steady-state and transient conditions. More in detail, the following tests were considered for the model calibration and assessment:

1. a full engine map, carried out with pilot injection/EGR and without pilot injection/EGR (Figure 3, red circles).
2. sweep tests of SOI_{main} (main injection timing) and p_f (injection pressure) carried out at selected key-points (Figure 3, black circles). In these tests, for each engine operating point, SOI_{main} and p_f were varied of ±6 deg and of ±20% around the nominal values, respectively. The pilot quantity and the dwell-time between the pilot and main pulses were maintained constant. These tests were carried out in torque control mode. These sweep tests were carried out with pilot injection/EGR and without pilot injection/EGR.
3. EGR- and VGT-sweep tests at fixed key-points (Figure 3, blue circles).

The total number of steady-state tests is of the order of 2200.

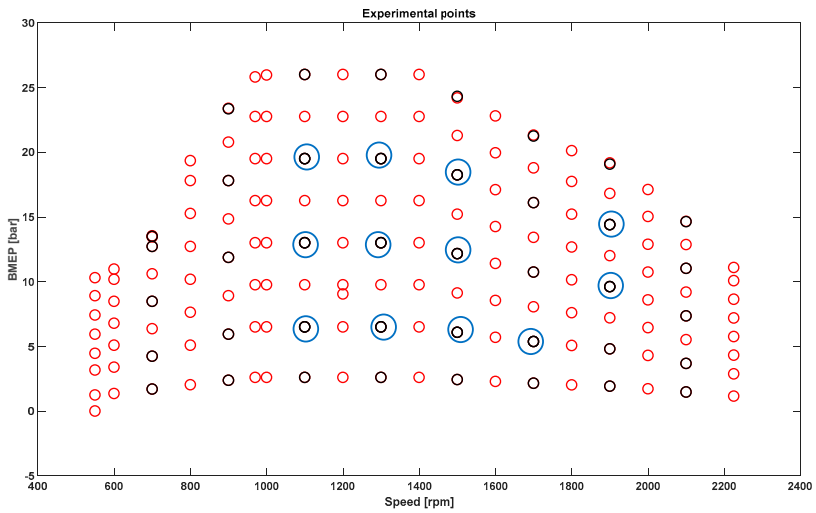

Figure 3. Summary of the experimental tests.

With reference to the transient tests, which were used for model validation, the details are reported in the "Results and Discussion" section.

With reference to the fuel used in the present investigation, the engine was fed with conventional diesel fuel (according to EN 590 regulations), whose main properties are listed in Table 4.

Table 4. Main properties of the diesel EN590 fuel.

Property	Units	Diesel EN 590 Class 0
Cetane number	-	54
Flash Point	°C	68
Density at 15 °C	kg/m^3	836
Density at 40 °C	kg/m^3	818
Viscosity at 20 °C	mm^2/s	4.49
Viscosity at 80 °C	mm^2/s	1.49
Lower heating value	MJ/kg	43.0

3. Model Description

The scheme of the real-time combustion model, as well as of the needed input variables, is reported in detail in Figure 4.

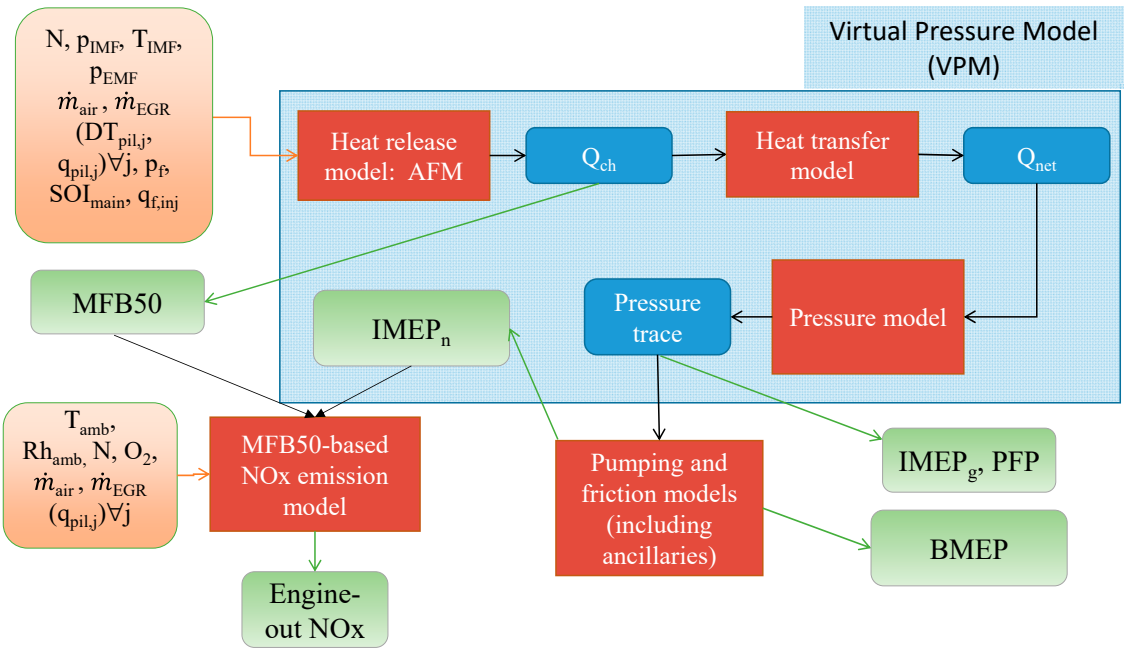

Figure 4. Scheme of the real-time combustion model.

In particular, in Figure 4, N indicates the engine speed, p_{IMF} and T_{IMF} the intake manifold pressure and temperature, respectively, p_{EMF} the exhaust manifold pressure, $\dot{m}_{air}$ and $\dot{m}_{EGR}$ the mass flow rate of fresh air and of EGR, respectively, $DT_{pil,j}$ the dwell-time of pilot injections, $q_{pil,j}$ the injected fuel quantity of the pilot injections, T_{amb} the ambient pressure, Rh_{amb} the ambient relative humidity, and $q_{f,inj}$ the total injected fuel quantity.

Basically, the heat release is evaluated first, on the basis of the accumulated fuel mass (AFM) approach. This allows the calculation of the chemical energy release (Q_{ch}) and of the related metrics (e.g., MFB50) to be performed.

Then, by using a heat transfer model, the net energy release (Q_{net}) is estimated, which in turn is used as input for the in-cylinder pressure model. The latter model is capable of estimating the

in-cylinder pressure trace and the related metrics, such as $IMEP_g$ (gross Indicated Mean Effective Pressure) and PFP (Peak Firing Pressure).

Finally, on the basis of friction (FMEP) and pumping (PMEP) models, the net IMEP ($IMEP_n$) and BMEP (Brake Mean Effective Pressure) are estimated.

With reference to the NO_x estimation, a slightly revised version of the approach described in ref. [26] was adopted. This model is based on the estimation of the deviations of NO_x emissions, with respect to the nominal engine-calibration map values, as a function of the deviations of the intake oxygen concentration and MFB50.

The detailed description of each submodel is reported in detail in previous papers (see [17,26]).

However, a summary of the equations is reported in Tables 5 and 6. It should be noted that the model tuning parameters have been underlined in the equations. In particular, Table 5 reports the equations of the chemical and net energy release models, while Table 6 reports the equation of the pressure and of the NO_x models.

Table 5. Main equations of the chemical and net energy release models. j indicates the generic injection pulse, K and τ are the combustion rate and ignition delay coefficients. $Q_{f,evap}$ and $Q_{ht,glob}$ indicate the fuel evaporation heat and the heat exchanged by the charge with the walls over the combustion cycle. $m_{f,inj}$ is the total injected fuel mass per cyc/cyl.

Q_{ch} Model	Q_{net} Model
$\frac{dQ_{ch,pil,j}}{dt}(t) = \underline{K_{pil,j}}[Q_{fuel,pil,j}(t-\underline{\tau_{pil,j}}) - Q_{ch,pil,j}(t)]$	$Q_{net,ht} \cong Q_{ch}\frac{m_{f,inj}H_L - Q_{ht,glob}}{m_{f,inj}H_L}$
$\frac{dQ_{ch,main}}{dt}(t) = \underline{K_{1,main}}[Q_{fuel,main}(t-\underline{\tau_{main}}) - Q_{ch,main}(t)] + \underline{K_{2,main}}\frac{dQ_{fuel,main}(t-\underline{\tau_{main}})}{dt}$	$Q_{net} \cong Q_{net,ht} - \underline{Q_{f,evap}}$
$Q_{fuel,j}(t) = \int_{t_{SOI,j}}^{t} m_{f,inj}(t)H_L dt \quad t \le t_{EOI,j}$	
$Q_{fuel,j}(t) = \int_{t_{SOI,j}}^{t_{EOI,j}} m_{f,inj}(t)H_L dt \quad t > t_{EOI,j}$	
$Q_{ch} = \sum_{j=1}^{n} Q_{ch,j}$	

Table 6. Main equations of the pressure and of the NO_x models. pIMF indicates the intake manifold pressure, pIVC the in-cylinder pressure at IVC, n and n′ the compression and expansion polytropic exponents. The combustion phase simulation derives from a single-zone heat release model [27].

Pressure Model	NO_x Model
Starting condition (p_{IVC}) : $p_{IVC} = p_{IMF} + \underline{\Delta p_{IMF}}$	$NOx = NOx_N(N, IMEP_n) + \delta NOx\left(\delta MFB50, \delta O_2, \frac{p_{IMF}}{q_{f,inj}}, NOx_N\right)$
Compression phase (IVC to SOC) : $pV^{\underline{n}} = const$	$\delta^{NOx} = \underline{a_1} \times \left[-abs(\delta MFB50)^{\underline{a2}} \times sign(\delta MFB50) + \underline{a_3}\delta O_2\right] \times \left(\frac{p_{IMF}}{q_{f,inj}}\right)^{\underline{a4}} \times NOx_N^{\underline{a_5}}$
Combustion phase (SOC to EOC): $p^i = \frac{\Delta Q_{net} - \frac{p^{i-1}}{2}(V^i - V^{i-1}) + \frac{1}{\gamma-1}p^{i-1}V^{i-1}}{\frac{V^i - V^{i-1}}{2} + \frac{V^i}{\gamma-1}} \; (\gamma = 1.4)$	$\delta MFB50 = MFB50 - MFB50_N(N, IMEP_n); \quad \delta O_2 = O_2 - O_{2N}(N, IMEP_n)$
Expansion phase (EOC to EVO) : $pV^{n'} = const$	
$IMEP_g = \frac{\int_0^{360} pdV}{V_0}$	
$IMEP_n = IMEP_g - \underline{PMEP}$	
$BMEP = IMEP_n - \underline{FMEP}$	

With reference to the NO_x model, it can be seen from Table 6 that the engine-out NOx emissions as the sum of two contributions: the nominal NO_x value 'NOx_N', which represents the emissions when the engine operates at nominal conditions, and an NO_x deviation term ('δNOx') which is null when MFB50 or intake O_2 concentration deviate with respect to the nominal engine map values $MFB50_N$ and O_{2N}.

The $\left(\frac{p_{IMF}}{q_{f,inj}}\right)^{\underline{a4}} \times NOx_N^{\underline{a_5}}$ term is a scaling factor which accounts for the fact that the range of NO_x deviations changes as a function of the engine operating points, even for constant deviations of MFB50 and intake O_2 concentration. The $p_{IMF}/q_{f,inj}$ term takes into account the effect of the air-to-fuel ratio

(AF). AF was not used directly since it is affected by a higher degree of uncertainty than that of the $p_{IMF}/q_{f,inj}$ term.

The nominal values of NO_x emissions, MFB50 and O_2 have been tabulated as a function of engine speed N and $IMEP_n$, and these tables are based on the measurements performed at steady-state conditions. Finally, it should be recalled that the NO_x model equations shown in Table 6 are valid for a given set of ambient temperature and humidity. If the model is applied to predict NO_x emissions when the ambient conditions are varied, the NO_x are corrected according to the recommended practice proposed in ref. [28]. The procedure is illustrated in ref. [26].

Estimation of the Intake O_2 Concentration

The intake O_2 concentration is a very important variable for the model, since it affects the combustion process and the NO_x formation process to a great extent.

When the model is assessed using the test bench data, an accurate measurement of O_2 is available, by means of the test bench gas analyzer.

However, if the model is used for onboard combustion control, this measurement is not available, and an alternative method is required to estimate it. Two approaches are possible for this purpose:

- The intake O_2 concentration is measured by means of an intake O_2 commercial sensor.
- The intake O_2 concentration is estimated on the basis of a sub-model.

In this paper, the impact of the method used to estimate the intake O_2 concentration on the model accuracy is investigated.

The following sub-model was used to estimate O_2 [29]:

$$O_2 = x_1 \frac{X_{r,EGR}}{RAF} + x_2 \tag{1}$$

where x_1, x_2 are fitting parameters, RAF is the relative air-to-fuel ratio, $X_{r,EGR}$ is the EGR rate.

The EGR rate $X_{r,EGR}$ is defined as follows:

$$X_{r,EGR} = \frac{m_{EGR}}{m_{EGR} + m_{air}} \tag{2}$$

where m_{EGR} is the trapped EGR mass and m_{air} is the trapped air mass.

The relative air-to-fuel ratio is defined as follows

$$RAF = \frac{AF}{AF_{st}} = \frac{m_{air}}{m_{f,inj} AF_{st}} \tag{3}$$

where m_{air} is the trapped air mass, $m_{f,inj}$ is the injected fuel mass, AF is the air-to-fuel ratio and AF_{st} is the stoichiometric air-to-fuel ratio (taken as 14.4 in this work).

In this study, RAF was estimated from an UEGO sensor, while the air and EGR mass were estimated from a sub-model embedded in the ECU. Details of these submodels cannot be provided for confidentiality reasons. However, the general approach is as follows:

- The total trapped mass is evaluated by estimating the volumetric efficiency of the engine
- The EGR mass is estimated using an approach based on the pressure differential across the EGR valve and the EGR valve opening position (see [29])
- The air mass is estimated as the difference between total trapped mass and EGR mass.

The average root means square error in the estimation of the EGR mass flow rate, at steady-state operation, is of the order of 24 kg/h, and the average root mean square error of EGR rate is of the order of 3% (absolute error). The EGR mass flow rate error was estimated by comparing the EGR mass flow rate estimated by the ECU with the EGR mass flow rate derived from the experimental measurements. In particular, the latter was calculated by means of Equation (2), where the experimental value of

$X_{r,EGR}$ was obtained on the basis of the intake and exhaust CO_2 concentrations, while the air mass flow rate was measured directly on the basis of the test bench sensors.

4. Model Calibration

Basically, the aim of the calibration phase is to identify physically-consistent correlations for the model calibration parameters, which have been underlined in Tables 5 and 6 and are listed in Table 7.

Table 7. Calibration parameters of the real-time combustion model.

Submodel	Calibration Parameter
Heat release model	$K_{pil,j}$; $K_{1,main}$; $K_{2,main}$; $\tau_{pil,j}$; τ_{main}
Net energy release model	$Q_{f,evap}$; $Q_{ht,glob}$
Pressure model	Δp_{IMF}; n; n′
BMEP model	PMEP; FMEP
NOx model	a_1; a_2; a_3; a_4; a_5

The model calibration was carried out according to the following steps.

- Heat release model: first, the experimental net and chemical heat release curves are derived on the basis of the measured in-cylinder pressure traces. Afterwards, the calibration parameters of the heat release model are tuned, test by test, in order to achieve the best possible matching between the predicted and experimental Q_{ch} profiles. A least square fitting algorithm is used to this aim. At the end of this phase, a dataset of optimal values of K and τ for all calibration tests is available. This dataset is used to derive physically-consistent correlations, as a function of significant engine variables. The selection of the input variables is done as a result of a trade-off between prediction accuracy (which takes benefit of a large number of input variables) and model robustness (which suffers from the adoption of a large number of variables).
- Net energy release model: the experimental values of $Q_{f,evap}$ and $Q_{ht,glob}$ are derived, for each calibration point, on the basis of the measured in-cylinder pressure and of the related net energy release. The dataset of optimal values of $Q_{f,evap}$ and $Q_{ht,glob}$ is then used to derive the physically-consistent correlations.
- Pressure model: the experimental values of Δp_{IMF}, n and n′ are derived, for each calibration point, on the basis of the analysis of the measured in-cylinder pressure trace. The dataset of optimal values is then used to derive the physically-consistent correlations.
- PMEP and FMEP models: the experimental values of PMEP and FMEP are derived, for each calibration point, on the basis of the measured in-cylinder pressure trace. In particular, PMEP is obtained from the analysis of the pressure curve during the gas exchange process, while FMEP is obtained as the difference between the pressure-derived $IMEP_n$ and the measured BMEP. The dataset of optimal values is then used to derive the physically-consistent correlations.
- NO_x model: the experimental values of the deviations δNO_x, δMFB50, and δO_2 are estimated, for each calibration point, on the basis of the test bench measurements. The coefficients of the NO_x model reported in Table 6 are then tuned on the basis of the least square method.

It should be noted that the indicated parameters for model calibration were extracted from one of the engine cylinders (i.e., cyl 1).

Therefore, any cyl-to-cyl variability of the main combustion or emission metrics is indirectly taken into account by the tuning of the model parameters. For example, consider the estimation of the FMEP parameter (see Table 6). During the model calibration phase, FMEP is estimated as the difference between the IMEP value of cyl 1 (which is derived from the in-cylinder pressure) and the BMEP value which is measured at the test bench. If cylinder 1 is characterized by a systematic higher performance than the other cylinders in terms of IMEP, this will result in an overestimation of FMEP with respect to the real value. As a consequence, the pressure model will provide a systematic overestimation of IMEP

with respect to the average value of the cylinders (being calibrated using the data of cyl. 1), and the friction model will provide a systematic overestimation of FMEP (being calibrated on experimental values which are overestimated). However, when the full model is applied to estimate BMEP, there will be a compensation of the effects, since the overestimation of IMEP provided by the model will be compensated by the overestimation of FMEP, and a correct calculation of BMEP will be obtained.

First, the model calibration was carried out by using the engine map tests and the SOI_{main}/p_f sweep tests (with and without EGR) shown in Figure 3. The VGT/EGR sweep-tests were instead used for the model assessment. With reference to the heat release model, some simplifications were done on the basis of the analysis of the heat release traces of the engine considered in this study. In particular, it was verified that the contribution of the pilot shot is very small, and the dwell-time between the pilot and main shots is generally short. Therefore, the start of combustion of the pilot shot was set equal to the start of combustion of the main pulse in order to simplify the calculations, and a single correlation was identified for the main ignition delay:

$$\tau[\mathrm{deg}] = 0.031 p_f^{-0.634} \rho_{SOI,main}^{-0.682} N^{1.500} \tag{4}$$

The following correlations were identified for the combustion rate parameters of the heat release model:

$$K_{1,main}[\frac{1}{\mathrm{deg}}] = 16.789 {p_f}^{0.305} \rho_{SOIM}^{0.074} N^{-0.663} q_{f,inj}^{-0.795} {p_{IMF}}^{0.979} \tag{5}$$

$$K_{2,main}[-] = 1.059E-03 p_f^{0.394} \rho_{SOIM}^{-0.980} O_2^{2.298} N^{-0.401} q_{main}^{0.483} \tag{6}$$

$$K_{pil}[\frac{1}{\mathrm{deg}}] = 0.01 \tag{7}$$

A constant value for K_{pil} was set, considering again its small contribution to the global heat release. With reference to the net energy release model, the following correlations were found:

$$Q_{f,evap}[kJ] = 8.65E-10 T_{IMF}^{0.705} N^{1.472} q_{f,inj}^{0.287} {SOI_{main}}^{0.817} {p_f}^{-0.376} \tag{8}$$

$$Q_{ht,glob}[kJ] = 2.863 {\rho_{SOIM}}^{-0.724} N^{-0.295} q_{f,inj}^{1.372} {O_2}^{-1.0196} \tag{9}$$

With reference to the pressure and BMEP models, the identified correlations are:

$$\Delta p_{IMF}[bar] = A_0\, p_{IMF}^{a_1} N^{a_2} \tag{10}$$

$$n = 3.084\, T_{IMF}^{-0.167} N^{0.020} {p_{IMF}}^{0.017} q_{f,inj}^{0.0017}\ (IVC \leq CA < 320^\circ) \tag{11}$$

$$n = 69.189 \cdot T_{IMF}^{-0.132} N^{-0.011} {p_{IMF}}^{0.014} SOI_{first}^{-0.561} (320^\circ \leq CA > SOI) \tag{12}$$

$$n\prime = 8.778 \times N^{-0.030} {q_{f,inj}}^{-0.046} {p_{IMF}}^{0.067} {SOI_{main}}^{-0.253} \tag{13}$$

$$PMEP[bar] = A_0 \cdot p_{EMF}^{a_1} N^{a_2} - B_0 \cdot p_{IMF}^{b_1} N^{b_2} \tag{14}$$

$$FMEP[bar] = a_0 \cdot N + a_1 \cdot N^2 + a_2 \cdot PFP + a_3 \tag{15}$$

$$O_2 = -21.94 \frac{X_{r,EGR}}{RAF} + 20.57 \tag{16}$$

It should be noted that the units of K and τ parameters are expressed as a function of the crank angle. This is due to the fact that the heat release model equations reported in Table 5 are implemented on a crank angle domain. It can be seen that two distinct correlations have been worked out for the polytropic coefficient n. In fact, for the present engine, it was noted that the pressure trace simulation and the accuracy in the estimation of IMEP can be largely improved when adopting two distinct definitions of the polytropic coefficient, the first one being used for the first part (IVC to 320°) and the second one for the last part (320° to pilot SOI) of the compression phase. In particular, it was verified

that using one constant value of the polytropic coefficient over the entire compression phase brought a systematic overestimation of IMEP, especially at high load conditions. The main reason is due to the fact that a large displacement engine, such as the C11 engine under study, typically features an injection pattern which includes a small pilot injection with relatively delayed SOI, with a short dwell time with respect to the main injection. As a consequence, the compression phase interval prior to the pilot SOI is quite long, and the thermal capacity of the charge varies over this interval, with a consequent variation in the value of the polytropic coefficient. It was verified that the introduction of two distinct values of the polytropic coefficients during the compression phase brought a reduction of the RMSE of IMEP with respect to the original approach. This can be seen in Table 8, which reports the RMSE of IMEP derived from the simulated pressure traces during the point-by-point calibration phase, using the two approaches. It can be seen that adopting two distinct values of n during the compression phase leads to significant improvement in the reconstruction of the in-cylinder pressure and IMEP estimation.

Table 8. RMSE of IMEP derived from the simulated pressure traces during the point-by-point calibration phase, when adopting a constant or two distinct definitions of the polytropic coefficient during the compression phase.

Number of Definitions for the 'n' Coefficient	Engine Map Tests w/o EGR	SOI_{main}/p_f Sweep Tests w/o EGR	Engine Map Tests with EGR	SOI_{main}/p_f Sweep Tests with EGR	EGR/VGT Sweep Tests
1	0.509 bar	0.517 bar	0.326 bar	0.317 bar	0.212 bar
2	0.193 bar	0.199 bar	0.109 bar	0.107 bar	0.073 bar

The numerical values of the coefficients of Equations (10), (14) and (15) are not reported for confidentiality reasons.

Finally, for that which concerns the NO_x model, the following formulation was identified for the NO_x deviation:

$$\delta NOx[ppm] = 0.024 \cdot \left[-abs(\delta MFB50)^{1.10} \cdot sign(\delta MFB50) + 3.85 \cdot \delta O_2\right] \cdot \left(\frac{p_{IMF}}{q_{f,inj}}\right)^{0.431} \cdot NOx_N^{1.39} \; (\delta MFB50 \geq 0) \quad (17)$$

$$\delta NOx[ppm] = 0.025 \cdot \left[-abs(\delta MFB50)^{1.270} \cdot sign(\delta MFB50) + 3.34 \cdot \delta O_2\right] \cdot \left(\frac{p_{IMF}}{q_{f,inj}}\right)^{0.499} \cdot NOx_N^{1.495} \quad (\delta MFB50 < 0) \quad (18)$$

5. Model-Based Combustion Controller

Within the IMPERIUM project, a model-based vehicle controller has been realized, which has the aim of optimizing the energy flows and the vehicle component operation, in order to achieve fuel consumption and urea consumption reduction of up to 20%. This is realized by means of an energy management supervisor, which is able to exploit real-time information concerning the traffic and the road characteristics, on the basis of a dynamic eHorizon system, so as to perform an on-board optimization of the vehicle operation. The energy manager supervisor is coupled with other model-based modules, including the ATS manager and the combustion controller, which was developed in this study. A scheme of the developed combustion controller is provided in Figure 5.

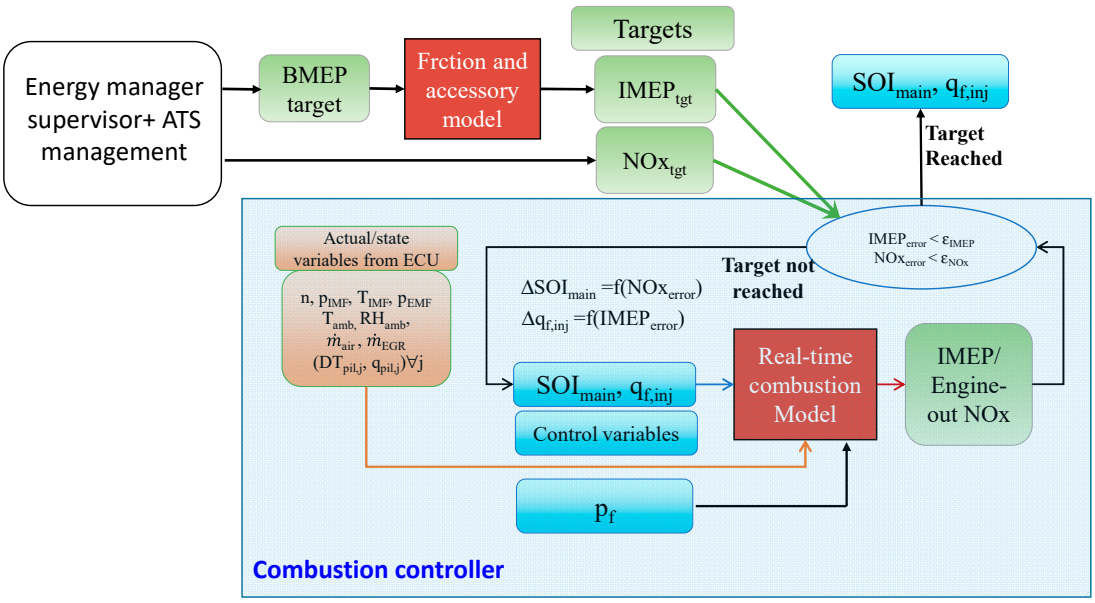

Figure 5. Scheme of the model-based controller of BMEP and NOx.

Basically, the combustion controller receives targets of engine-out NO_x (NOx_{tgt}) and net IMEP ($IMEP_{tgt}$) which are requested in real-time by the energy manager supervisor and the ATS management module, and predicts the values of the injected fuel quantity $q_{f,inj}$ and of the injection timing of the main pulse, i.e., SOI_{main}, that allow the desired targets to be achieved. This is done through an iterative procedure, which is performed within the engine cycle and which stops when the difference between the predicted and the required values of the target variables fall below the predefined thresholds ε_{IMEP} and ε_{NOX}. During the iterative procedure, SOI_{main} is corrected on the basis of the NO_x error, while $q_{f,inj}$ is corrected on the basis of the IMEP error. The injection pressure p_f is also corrected, with respect to the baseline value, using a correction map which is a function of the engine speed and load, in order to compensate for the soot increase that would be obtained when SOI_{main} is delayed to achieve low targets of NO_x emissions.

The proposed controller structure derives from that proposed in ref. [7], which had been developed for a 3.0 L diesel engine but not yet assessed for the implementation on a real engine. However, several improvements were made in comparison with the previous version in order to speed-up the convergence and improve its robustness in view of the implementation on the engine. The first difference is that the previous controller was based on a higher computationally demanding NO_x model, which required a 3-zone thermodynamic approach, while the new controller is based on the new NO_x model [26], which is much simpler and requires a shorted computational time.

The correction algorithm of $q_{f,inj}$ is the same as that described in ref. [7], i.e.,:

$$q^{j}_{f,inj,i+1} = q^{j}_{f,inj,i} + K^{j}_{IMEP,i} \cdot S^{j}_{IMEP,i} \cdot Err^{j}_{IMEP,i} \tag{19}$$

where 'j' indicates 'the generic engine cycle, 'i' indicates the iteration, $Err^{j}_{IMEP,i}$ is the BMEP error at cycle 'j' and iteration 'i' (i.e., the difference between the target value and the predicted value), $K^{j}_{IMEP,i}$ is a modulation factor, which was introduced in order to optimize the response of the controller and to guarantee stable operations, $S^{j}_{IMEP,i}$ is an fuel-to-IMEP sensitivity factor which is derived from the average engine fuel conversion efficiency. It was shown in ref. [7] that the modulation factor $K^{j}_{IMEP,i}$ varies in the [0.2, 1] range, and its value is halved if the sign of the IMEP error changes between two consecutive iterations, or is doubled otherwise.

With reference to the SOI_{main} correction, a new algorithm was proposed, which exploits the low-throughput capability of the NO_x model used for the present application and its dependency

on MFB50 (see Table 6). Basically, for a given NO_x target at cycle 'j' (i.e., NOx^j_{tgt}) an MFB50 sweep is built, which includes MFB50 variations of 0.1°, 1°, 3°, and 6° with respect to the nominal value of the current engine point. The NO_x model is then applied for all of the sweep points, keeping all the other parameters constant, and the related NO_x emissions are estimated for each MFB50 variation. Finally, using the results of the simulated sweeps, the value of MFB50 variation which leads to the desired target of NO_x (i.e., ΔMFB50*) is found by means of interpolation, and is used to correct SOI_{main}:

$$SOI^j_{main,i+1} = SOI^j_{main,i} + \Delta MFB50* \tag{20}$$

It was verified that the adoption of this correction schemes allows the target of NO_x to be achieved in a low number of iterations.

The use of the new NO_x model also brings an improvement of robustness and accuracy when using real time ECU signals as input. In fact, the previous 3-zone-based NO_x model, despite a similar performance when calibrated and validated using accurate input signals, showed a deterioration of accuracy when ECU-estimated input variables were used, due to its great sensitivity to the EGR and air mass.

Finally, several additional improvements were made in order to improve robustness and increase the resistance to input variables estimation failures, in view of the implementation on a real engine, such as:

- Introduction of upper/lower saturation for all the input variables
- Introduction of boundary safety limits for SOI_{main} and $q_{f,inj}$. In particular, the SOI_{main} boundary depends on engine speed and load, the $q_{f,inj}$ boundary is constant. These boundaries are introduced in order not to exceed the engine limits in terms of peak firing pressure and exhaust gas temperatures.
- Introduction of low thresholds of engine speed and injected fuel quantity, beyond which the controller is deactivated and the engine runs in standard ECU-based mode. This was done in order to improve robustness during the engine start phase and during the transitions from positive brake torque to cut-off conditions.
- Introduction of an output buffer for the control variables SOI_{main} and $q_{f,inj}$, which allows a smoothing of the trends before being sent to the engine ECU.

6. Results and Discussion

In this section the real-time combustion model is assessed and validated at both steady-state (Section 6.1) and transient (Section 6.2) conditions.

Section 6.3 reports instead a model robustness analysis, in order to verify the effect of the input parameter uncertainty on the accuracy of the model outcomes.

Section 6.4 is focused on a calibration sensitivity analysis, in order to check the effect of the number of type of calibration data on the model accuracy. This analysis demonstrates that the proposed model is robust even when a low number of points is used for calibration, thus it is physically consistent.

Section 6.5 reports the results of the computational time that is required by the model when it runs on an ETAS ES910 rapid prototyping device. This check is mandatory in order to verify the possibility to adopt the proposed model for the development of a model-based controller.

Finally, Section 6.6 reports a preliminary assessment of the functionality of the model-based controller.

6.1. Model Assessment at Steady-State Conditions

First, the model was assessed for the steady-state tests reported in Figure 3. It should be noted that the model performance is affected by the quality of the input parameters to a great extent. In order to verify this effect, three cases were considered:

- All the input variables are the result of the measurement of the test bench sensors (best case)

- The input variables are derived from the engine sensors or from the sub-models embedded in the ECU, except for the intake O_2 concentration
- All the input variables are derived from the engine sensors or from the sub-models embedded in the ECU.

For the three considered cases, Figure 6 reports the predicted vs. experimental levels of the indicated quantities, i.e., MFB50 (Figure 6a–c), normalized PFP (Figure 6d–f), and $IMEP_n$ (Figure 6g–i), while Figure 7 reports the predicted vs. experimental values of BMEP (Figure 7a–c) and engine-out NO_x emissions (Figure 7d–f). The experimental NO_x levels were obtained from the engine test cell gas analyzer. The prediction accuracy of each model was quantified by the squared correlation coefficient (R^2) and by the Root Mean Squared Error (RMSE), which are reported in each figure. With reference to Figure 7d–f, the lines corresponding to ±20% with respect to the bisector have also been reported, in order to better analyze the error of the NO_x model. The PFP values were normalized for confidentiality reasons.

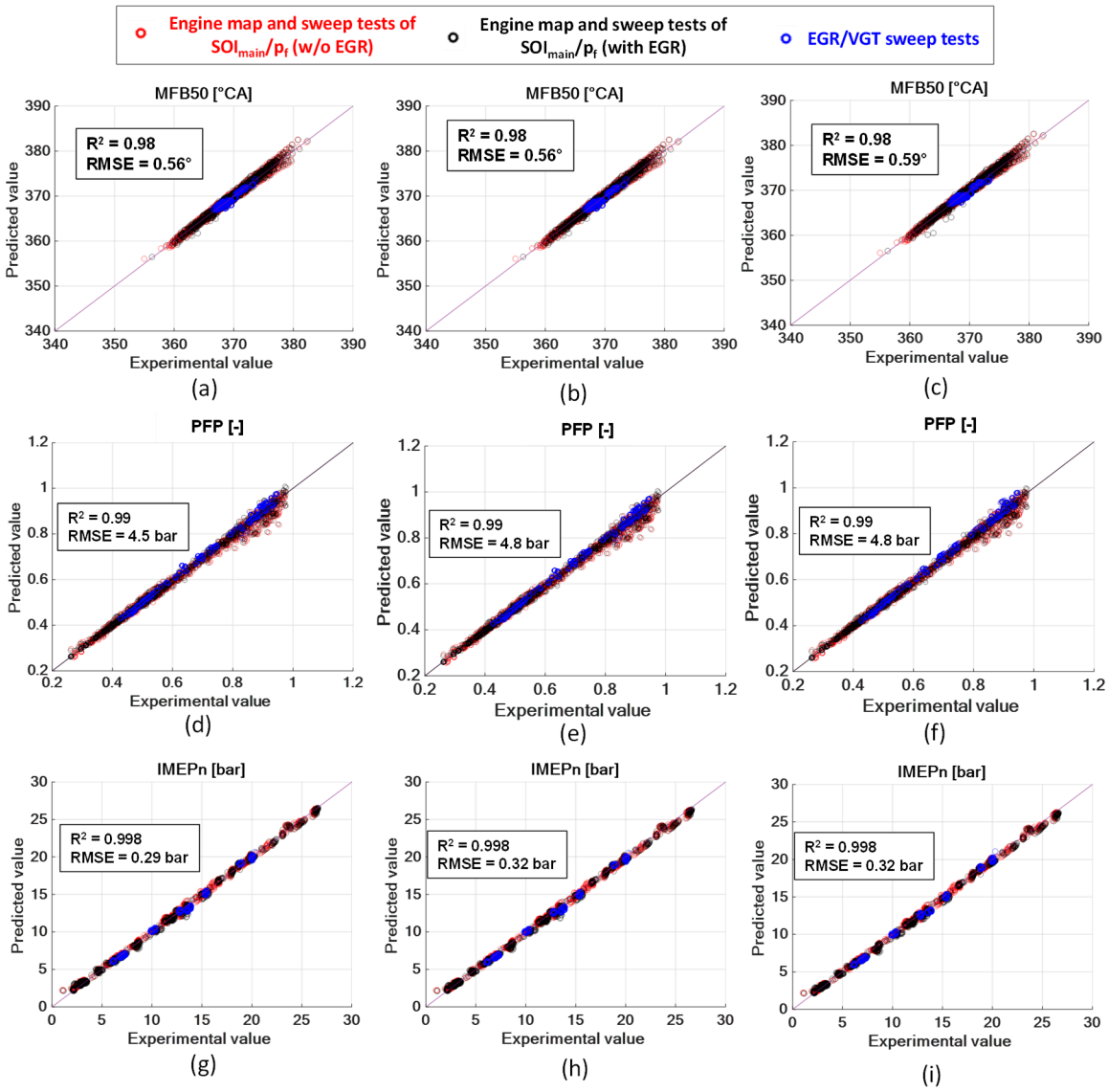

Figure 6. Predicted vs. experimental values of MFB50 (**a**–**c**), normalized PFP (**d**–**f**) and $IMEP_n$ (**g**–**i**) for the steady-state tests reported in Figure 3. (**a**,**d**,**g**): input variables from test bench sensors; (**b**,**e**,**h**): input variables from ECU sensors/models except for intake O_2; (**c**,**f**,**i**): input variables from ECU sensors/models.

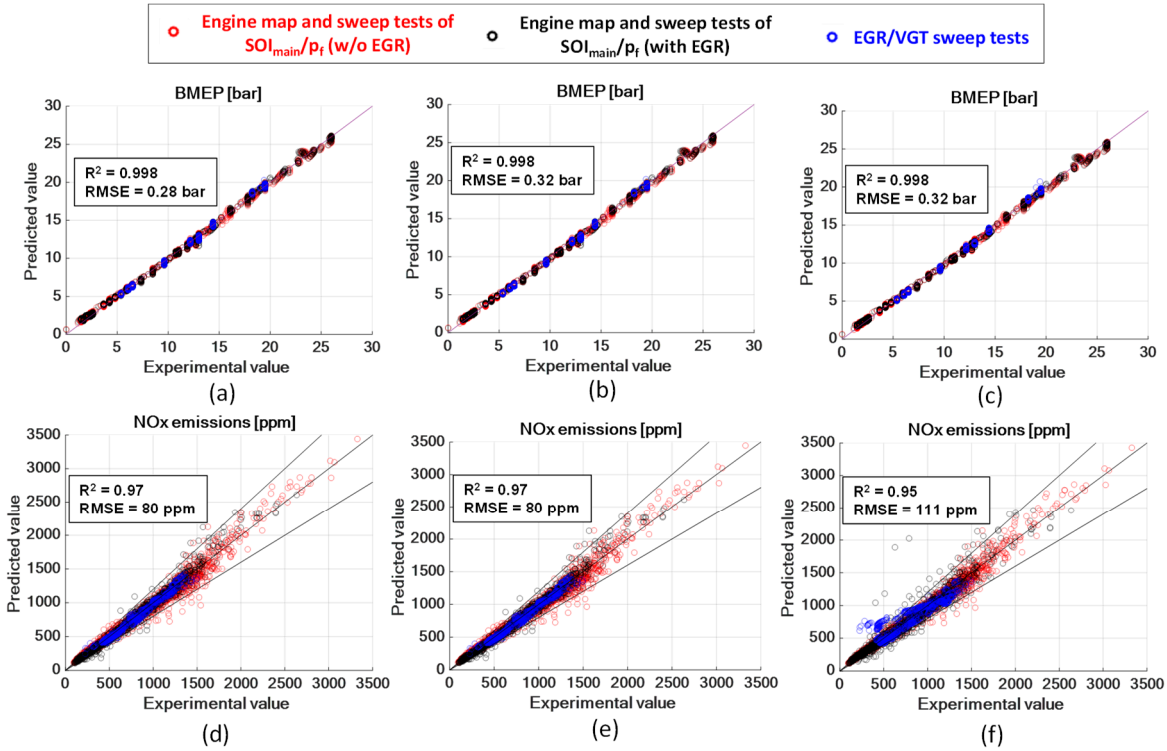

Figure 7. Predicted vs. experimental values of BMEP (**a**–**c**) and NO_x emissions (**d**–**f**) for the steady-state tests reported in Figure 3. (**a**,**d**): input variables from test bench sensors; (**b**,**e**): input variables from ECU sensors/models except for intake O_2; (**c**,**f**): input variables from ECU sensors/models.

The tests indicated in red refer to the engine map tests and SOI_{main}/p_f sweep tests without EGR, the tests indicated in black refer to the engine map tests and SOI_{main}/p_f sweep tests with EGR and finally tests indicated in blue refer to the VGT/EGR sweep tests.

It can be seen in the figures that, in general, the accuracy of the model is good. It was verified that the error distributions are centered around 0 for all parameters and feature Gaussian-like shapes (not shown here for the sake of brevity). Moreover, the accuracy in the estimation of MFB50, PFP, $IMEP_n$, and BMEP parameters is slightly affected when ECU-derived input parameters are used instead of bench-derived parameters.

With reference to NO_x estimation, the RMSE of the model is of the order of 80 ppm when the input variables are estimated from test bench sensors, and it is not affected if they are obtained from ECU sensors except for intake O_2 (see Figure 7e). However, if the ECU model is used to estimate the intake O_2 concentration (Figure 7f), the RMSE of the NO_x model increases to 111 ppm.

Table 9 shows the values of RMSE of the NO_x model for the three types of tests, in the two cases in which the input quantities are taken from the test bench sensors and from the ECU sensors or models.

Table 9. RMSE of the NO_x model for the three types of tests, in the two cases in which the input quantities are taken from the test bench sensors and from the ECU sensors or models.

Type of Test	Input Variables from Bench Sensors	Input Variables from ECU Sensors/Models
Engine map and sweep tests of SOI_{main}/p_f without EGR	101 ppm	95 ppm
Engine map and sweep tests of SOI_{main}/p_f with EGR	75 ppm	117 ppm
EGR/VGT sweep tests	44 ppm	127 ppm

It can be seen in Table 9 that the accuracy is almost unaffected for the tests without EGR, while the RMSE increases significantly for the tests featuring EGR when using the ECU-derived sensors or models, mainly as a consequence of the inaccuracy of the EGR model embedded in the ECU.

The previous results suggest that the adoption of an intake O_2 sensor is recommended for model-based combustion control applications, in order to keep the accuracy of the NOx model at a high level.

6.2. Model Validation over Transient Conditions

After the assessment at steady-state operation, the model was then validated in transient operation. The results reported in this section are related to two different transient tests. The first test type is constituted by a series of tip-in and tip-out load maneuvers at N = 1500 rpm. The second test type is constituted by a series of up/down load ramps at N = 1900 rpm. Each type of test was carried out with and without EGR. Figures 8 and 9 report the results of the tip-in and tip-out maneuvers without (Figure 8) and with (Figure 9) EGR, while Figures 10 and 11 report the results of the load ramps without (Figure 10) and with (Figure 11) EGR. In each figure, the time histories of the predicted (blue) and experimental (red) values of MFB50 (Figures 8a, 9a, 10a and 11a), normalized PFP (Figures 8b, 9b, 10b and 11b), BMEP (Figures 8c, 9c, 10c and 11c) and NO_x emissions (Figures 8d, 9d, 10d and 11d) are reported. The experimental NOx levels were obtained from the engine NO_x sensor. The values of R^2 and RMSE are also reported in each chart. With reference to the NO_x emissions, two modeled curves are reported: the light-blue trace refers to the raw model output ("Model"), while the blue trace was obtained by filtering the raw model output using a cut-off frequency of 0.66 Hz ("Model filt"). This filtering was adopted in order to better compare the model outcomes with the experimental trace obtained from the engine NO_x sensor, since the latter is characterized by a certain degree of smoothing and delay due to the response time of the sensor and of the mixing of the gases in the exhaust manifold. The PFP values were normalized for confidentiality reasons.

With reference to the experimental indicated quantities (MFB50 and PFP), they were processed and obtained directly from the test bench acquisition system.

With reference to the tip-in and tip-out load maneuvers (Figures 8 and 9), it can be seen from the charts that the average errors of MFB50, PFP, and BMEP are of the order of 1.6–1.7 degree, 6 bar, and 0.46–0.48 bar, respectively, and these errors are slightly influenced by the use of EGR. On the contrary, the prediction accuracy of NO_x emissions is strongly influenced by the use of EGR. In fact, it can be seen that when EGR is not adopted (Figure 8d), a very good matching is obtained between the predicted and experimental trace, especially if the filtered model trend is taken, with a value of RMSE of the order of 85 ppm. On the contrary, when EGR is adopted, the model accuracy deteriorates (the RMSE value is of the order of 305 ppm for the filtered model trace). It can be seen in Figure 9d that the model over predicts NO_x emissions at the end of the tip-in maneuver, while the experimental trace shows a drop of NO_x emissions in the same intervals. The main reason is due to the fact that the EGR model embedded in the ECU, although being accurate at steady-state operation, is not able to capture highly transient phenomena which occur in the intake manifold: as a consequence, the intake O_2 concentration, given to the NO_x model as input, is much higher that the real one, and the model over predicts the NO_x levels. An improvement of the EGR model embedded in the ECU, or the installation of an intake O_2 sensor may lead to significant improvements in the estimation of the NOx emissions when EGR is adopted.

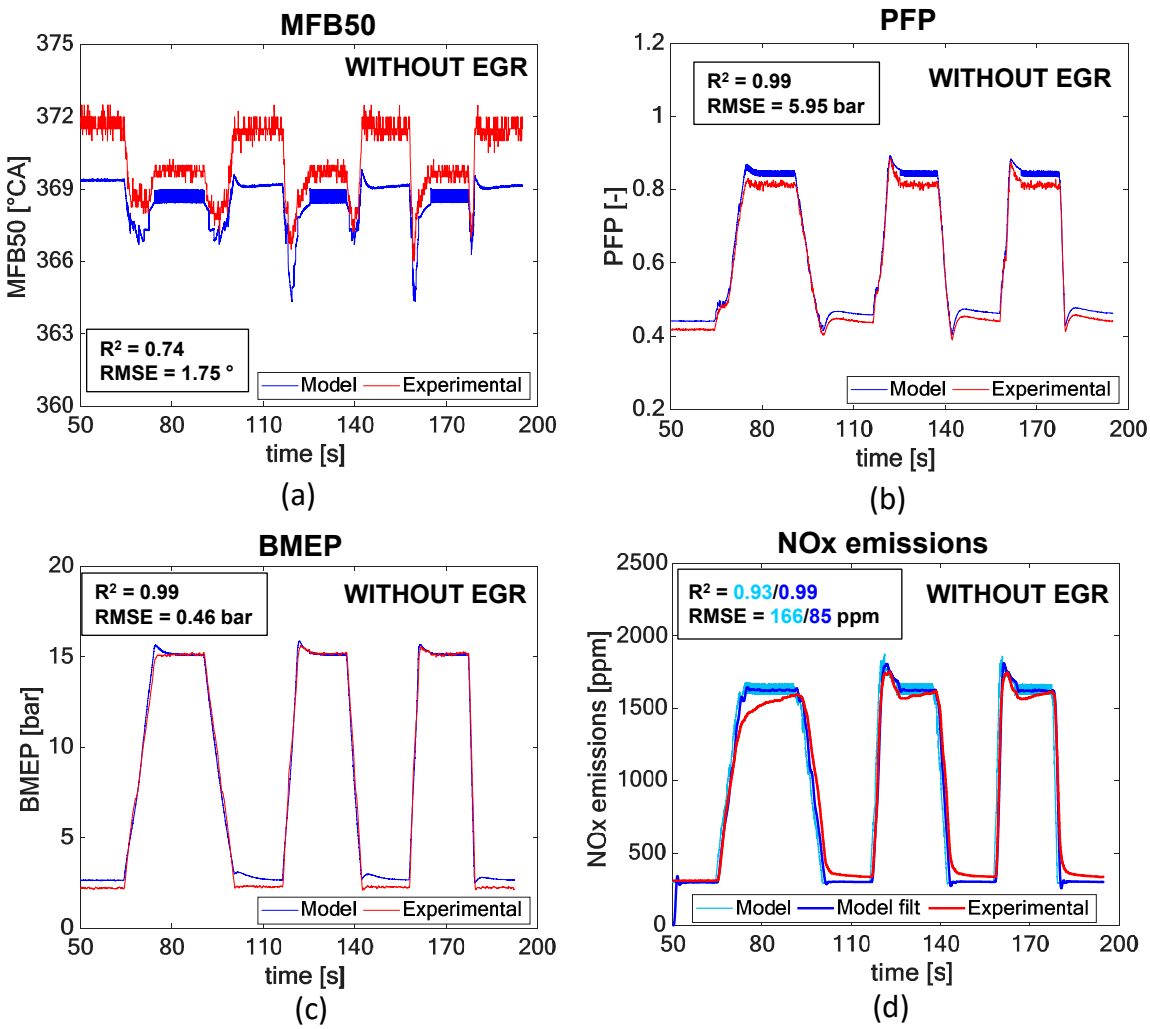

Figure 8. Predicted and experimental trends of MFB50 (**a**), normalized PFP (**b**), BMEP (**c**), and engine-out NO_x emissions (**d**) for the tip-in/tip-out load maneuvers at 1500 rpm, without EGR. The RMSE values are also reported.

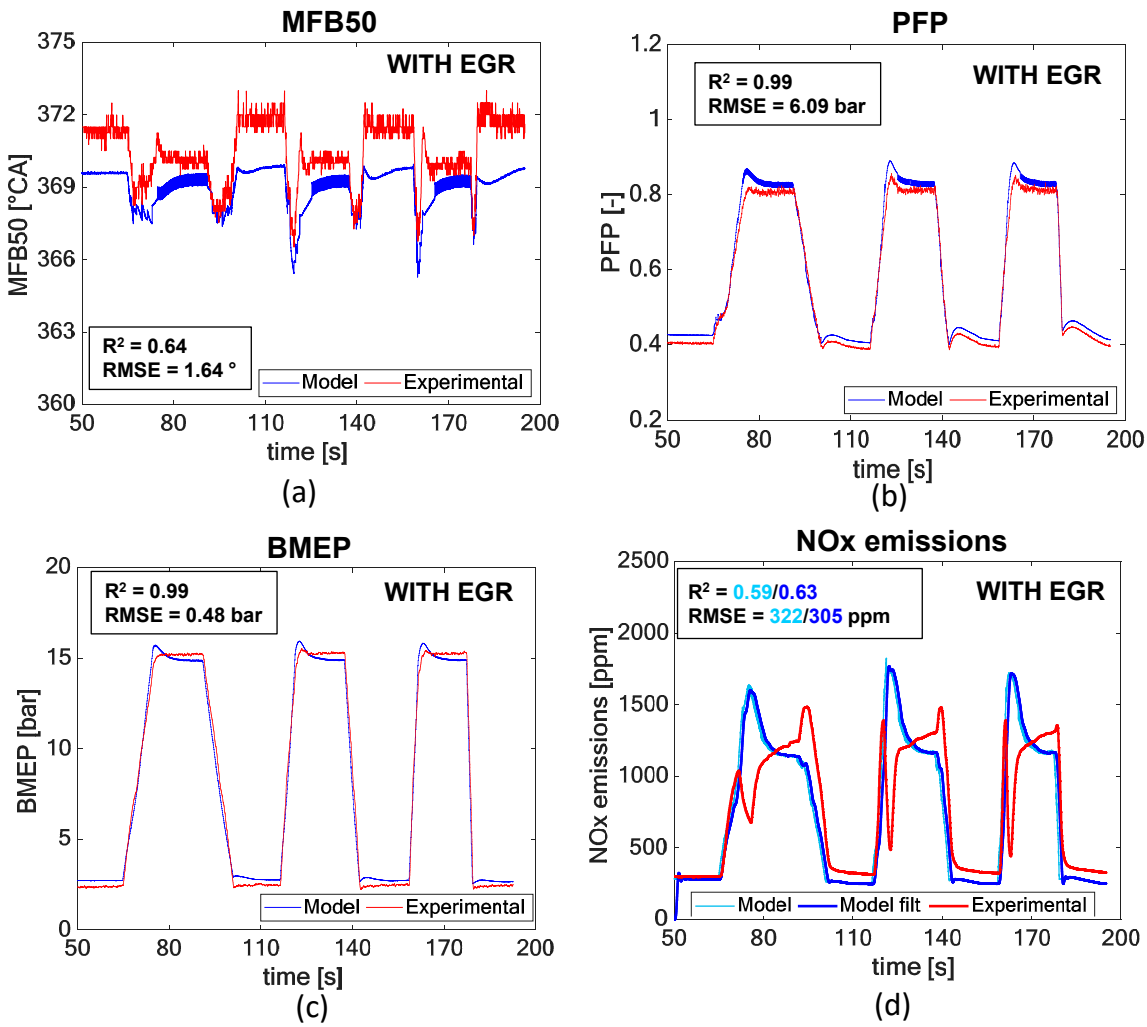

Figure 9. Predicted and experimental trends of MFB50 (**a**), normalized PFP (**b**), BMEP (**c**), and engine-out NO_x emissions (**d**) for the tip-in/tip-out load maneuvers at 1500 rpm, with EGR. The RMSE values are also reported.

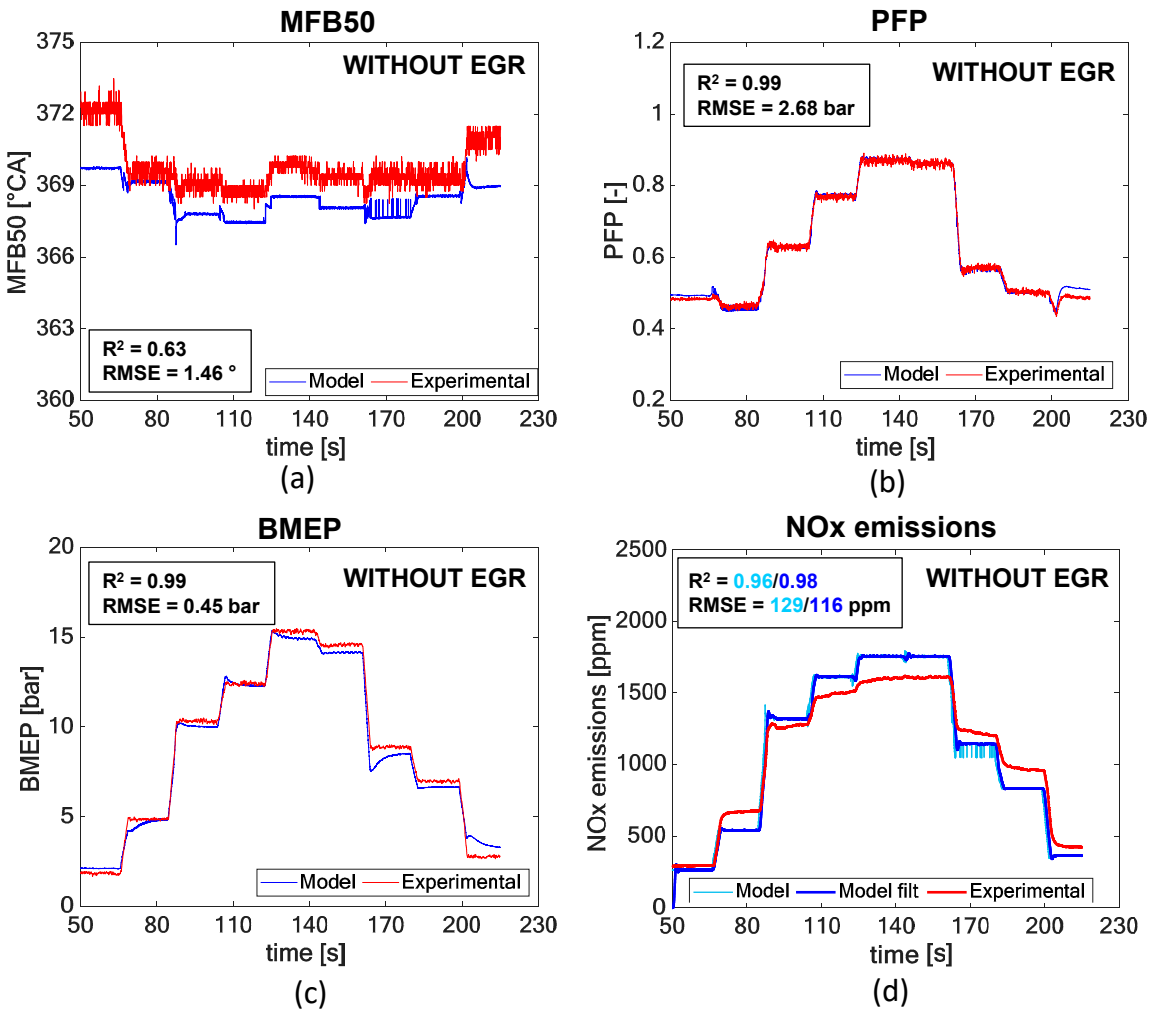

Figure 10. Predicted and experimental trends of MFB50 (**a**), normalized PFP (**b**), BMEP (**c**), and engine-out NO_x emissions (**d**) for the load ramp tests at 1900 rpm, without EGR. The RMSE values are also reported.

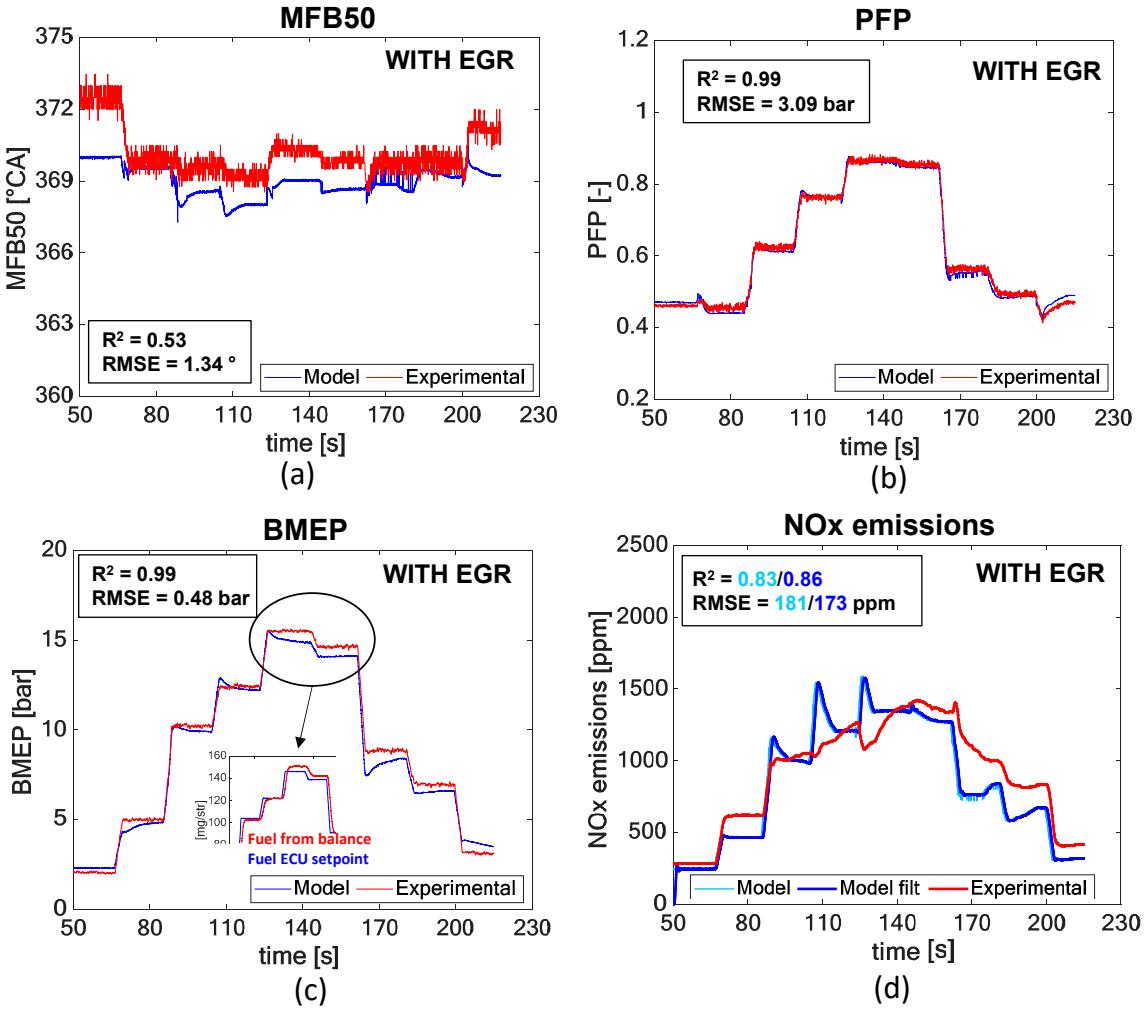

Figure 11. Predicted and experimental trends of MFB50 (**a**), PFP (**b**), BMEP (**c**), and engine-out NO_x emissions (**d**) for the load ramp tests at 1900 rpm, with EGR. The RMSE values are also reported.

With reference to the load ramps (Figures 10 and 11), a similar behavior of the model can be observed compared to that for the tip-in/tip-out maneuvers. In fact, it can be seen from the charts that the average errors of MFB50, PFP, and BMEP are of the order of 1.3–1.4 degree, 2.7–3 bar, and 0.45–0.48 bar, respectively, and these errors are slightly influenced by the use of EGR. The NO_x model is characterized by a good accuracy when EGR is not adopted (Figure 10d, RMSE = 116 ppm for the filtered model trace) and by a lower accuracy when EGR is adopted (Figure 11d, RMSE = 173 ppm for the filtered model trace). Also in this case, it can be observed that the model over predicts NO_x emissions at the end of the load ramps, as a consequence of an overestimation of the intake O_2 concentration during those phases.

With reference to the BMEP error, it is interesting to note that a significant contribution may be related to the uncertainty in the fuel quantity which is realized by the injectors with respect to the desired one. This can be verified in Figure 11c, which shows a comparison between the fuel quantity measured from the fuel meter (red line in the small box) and the ECU fuel setpoint (blue line in the small box). The ECU-derived fuel setpoint quantity was given to the model as input, and this can justify the BMEP underestimation in the considered time interval. The fuel quantity of the balance could not be used over the transients, due to a slow response in time.

On the basis of these results, an improvement of the accuracy of the injector maps is currently being performed using test bench results.

6.3. Model Robustness Analysis

A model robustness analysis has been carried out in this section, considering the steady-state tests reported in Figure 3. In particular, the procedure that was followed is reported hereafter.

- Combined variations numbering 2000 of the main model input variables were generated according to a Gaussian distribution, in which the standard deviation of each parameter was set according to the accuracy of the engine sensors or of the models used to estimate the parameters (see Table 10).
- The simulation of the steady-state points was performed considering all the 2000 combined variations of the main model input variables.
- The distribution of the RMSE values of the main model outcomes was evaluated.

Table 10. Standard deviation of the main model input variables.

Input Model Parameter	Description	Standard Deviation σ
p_{IMF}	Intake manifold pressure	0.33% of read value
T_{IMF}	Intake manifold temperature	0.33 °C
p_{EMF}	Exhaust manifold pressure	0.33% of read value
m_{air}	Trapped air mass	2.2E-1 g/stroke
m_{EGR}	Trapped EGR mass	1.1E-1 g/stroke
$q_{f,inj}$	Injected fuel quantity	6 mm^3
p_f	Injection pressure	0.0033% of read value
SOI_{main}	Start of injection of the main pulse	0.067° CA
T_{amb}	Ambient temperature	0.33°
Rh_{amb}	Ambient relative humidity	0.67% of read value

The results of this analysis are reported in Figure 12.

It can be seen that the most frequent values of RMSE are aligned with respect to the results shown in Figures 6 and 7, and that the maximum values of RMSE for the worst cases are of the order of 1.2 degree for MFB50, 6.5 bar for PFP, 1.4 bar for $IMEP_n$ and BMEP, and 250 ppm for the NO_x emissions. It was verified that the main variable which affects the RMSE of $IMEP_n$ and BMEP is the injected fuel quantity, while the main variables which affect the RMSE of NO_x emissions are the air and EGR mass. Therefore, an effort should be made in order to increase the accuracy of the injectors in realizing the desired fuel quantity and the accuracy of the submodels that estimate the air and EGR mass, in order to increase the robustness of the model. With reference to NO_x simulation, it could also be beneficial to install an intake O_2 sensor in order to replace the sub-models of air and EGR mass.

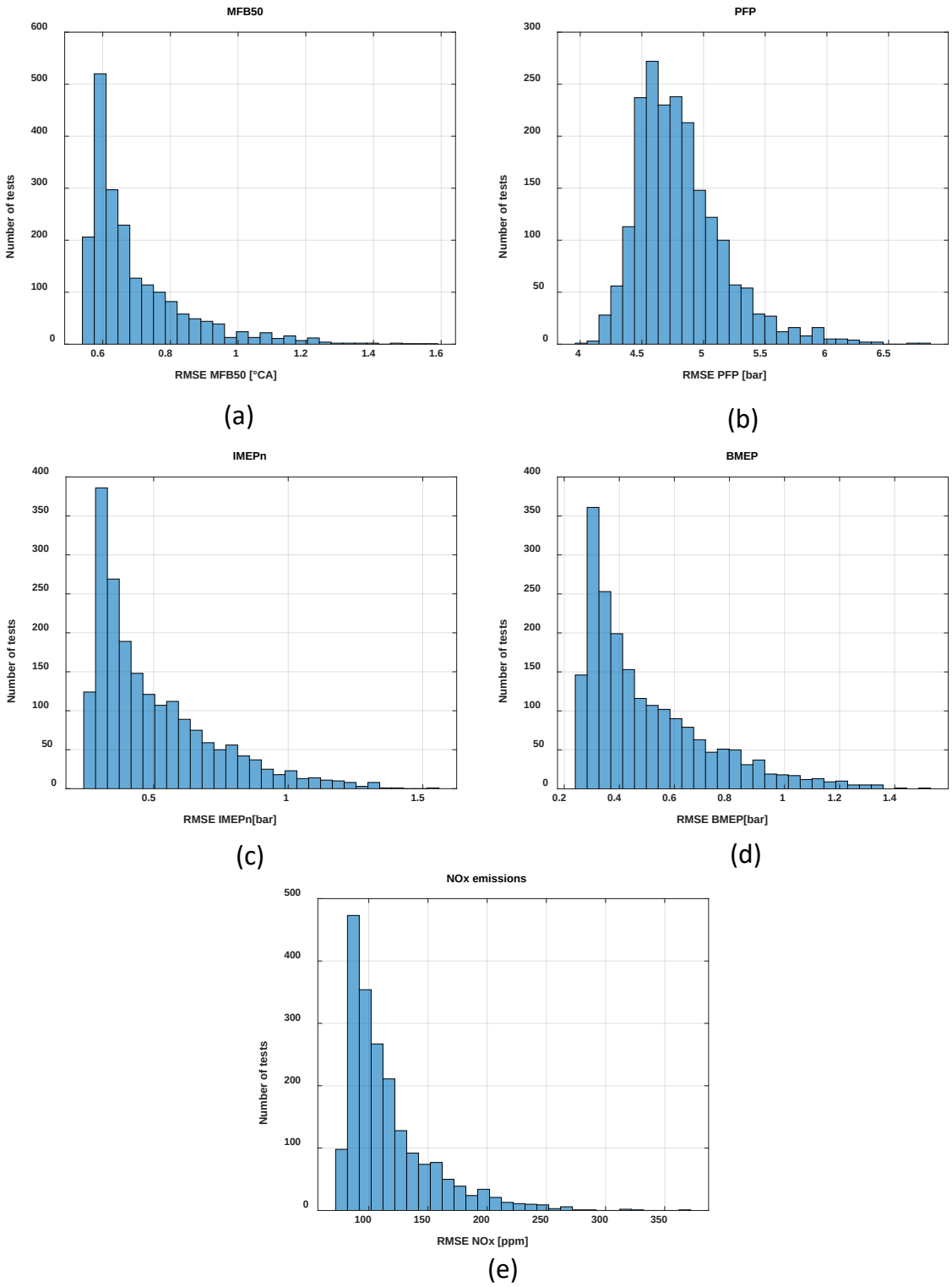

Figure 12. Distributions of the RMSE values of (**a**) MFB50; (**b**) PFP; (**c**) $IMEP_n$; (**d**) BMEP; and (**e**) NO_x emissions, when performing 2000 model simulations with input parameter deviations according to the standard deviations shown in Table 5.

6.4. Model Calibration with Limited Number of Experimental Tests

A calibration sensitivity analysis is carried out in this section. In particular, the original calibration dataset was progressively reduced and the accuracy of the resulting model checked over the entire dataset.

The reduced calibration datasets are shown in Figure 13 and were identified as follows:

- Reduced calibration dataset 1: the engine map tests were reduced to 50% of the original dataset as shown in Figure 13a,b; the SOI_{main}-p_f sweep tests were reduced by taking the maximum and minimum values of SOI_{main} and p_f for each engine point, as well as additional tests as shown in Figure 13c (an example is reported in Figure 13c for the 900 × 2.4 engine point).
- Reduced calibration dataset 2: the engine map tests were reduced to 20% of the original dataset as shown in Figure 13a,b; the SOI_{main}-p_f sweep tests were reduced by taking only the maximum and minimum values of SOI_{main} and p_f for each engine point, as well as the central point (see Figure 13c).

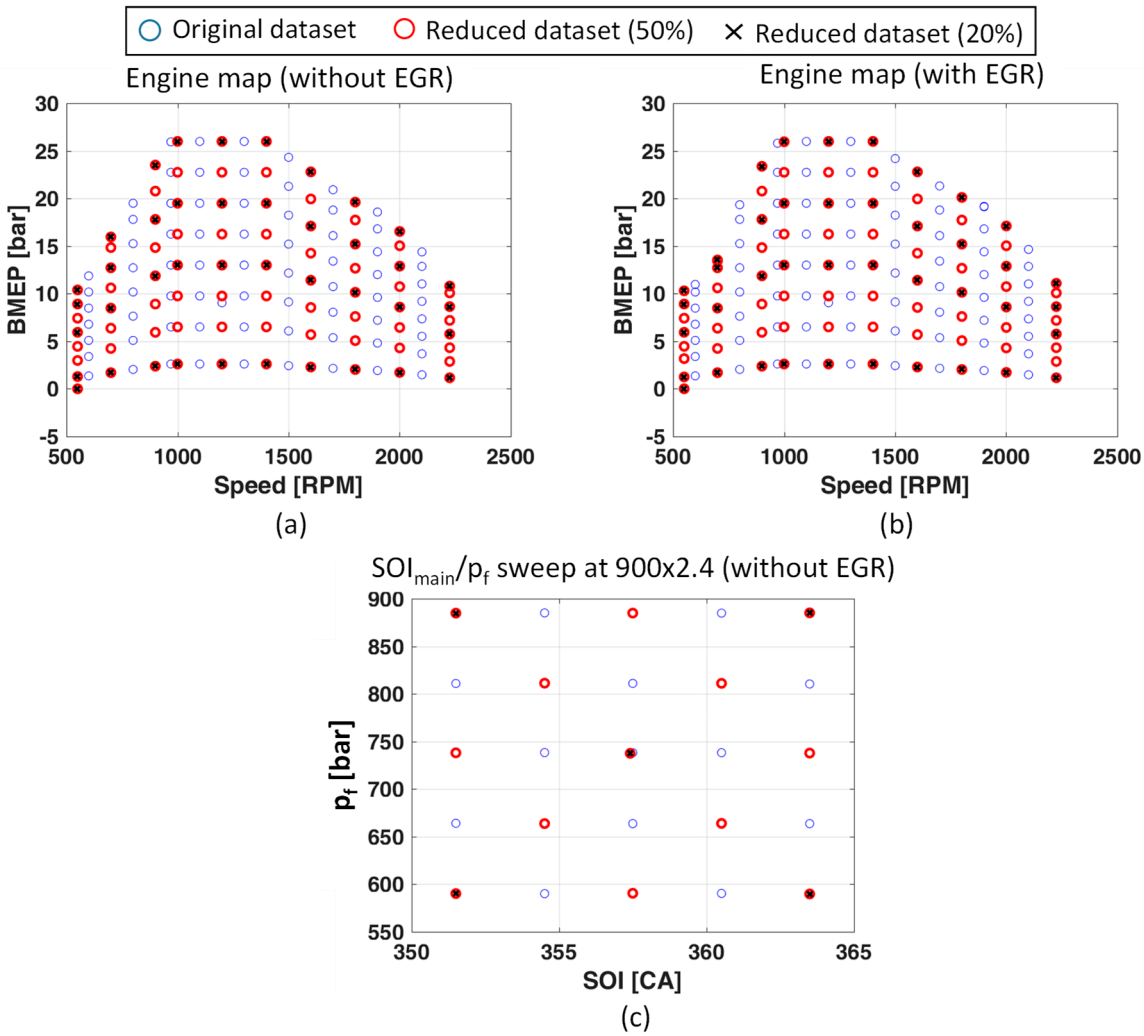

Figure 13. Reduction of the number of calibration points with reference to the engine map tests (**a**,**b**) and SOI_{main}-p_f sweep tests (**c**, an example is reported for the 900 × 2.4 engine point).

The model was tuned for each reduced dataset, and applied to the whole dataset, and the accuracy was estimated on the basis of the RMSE parameter. The result of this analysis is reported in Table 11 for the steady-state tests of Figure 3.

Table 11. Values of RMSE of the main model outcomes, for the different calibration datasets, when applying the model to the steady-state tests reported in Figure 3.

Calibration Datasets	MFB50 RMSE	PFP RMSE	$IMEP_n$ RMSE	BMEP RMSE	NOx RMSE
Original	0.559	4.507	0.289	0.281	80.0
Reduced (50% of original)	0.557	4.495	0.286	0.279	79.4
Reduced (20% of original)	0.569	4.481	0.284	0.274	79.1

It can be observed in the tables that the model accuracy is virtually unaffected by the reduction of the number of calibration points. This indicates that the model is physically consistent since it does not require a large number of points in order to obtain an accurate calibration (20% of the original dataset proposed in Figure 3 is sufficient). Moreover, it can be noted that, in addition to the engine maps, detailed sweep tests of the main engine parameters (SOI_{main}, p_f, . . .) are not required, since the use of the boundary values (i.e., the maximum and minimum values of the variation ranges) is sufficient.

6.5. Required Computational Time on ETAS ES910

The model was developed in the Matlab/Simulink environment and was then implemented on a rapid prototyping (RP) device (i.e., ETAS ES910), through ETAS Intecrio software.

The aim of this investigation was to test the real-time capability of the combustion model, for the subsequent development of the model-based controller.

The average computational time required by the model on the ETAS ES910 device is of the order 300–400 µs, when a crank angle integration step of 1 degree is used. Therefore, the model features real-time capability.

6.6. Assessment of the Model-Based Combustion Controller at Steady-State Conditions

The model-based combustion controller was preliminary assessed at steady-state conditions. Basically, the experimental values of IMEP and NO_x emissions were set as targets of the controller, and the values of $q_{f,inj}$ and SOI_{main} calculated by the controller were compared to the real actuated values. The results are shown in Figure 14.

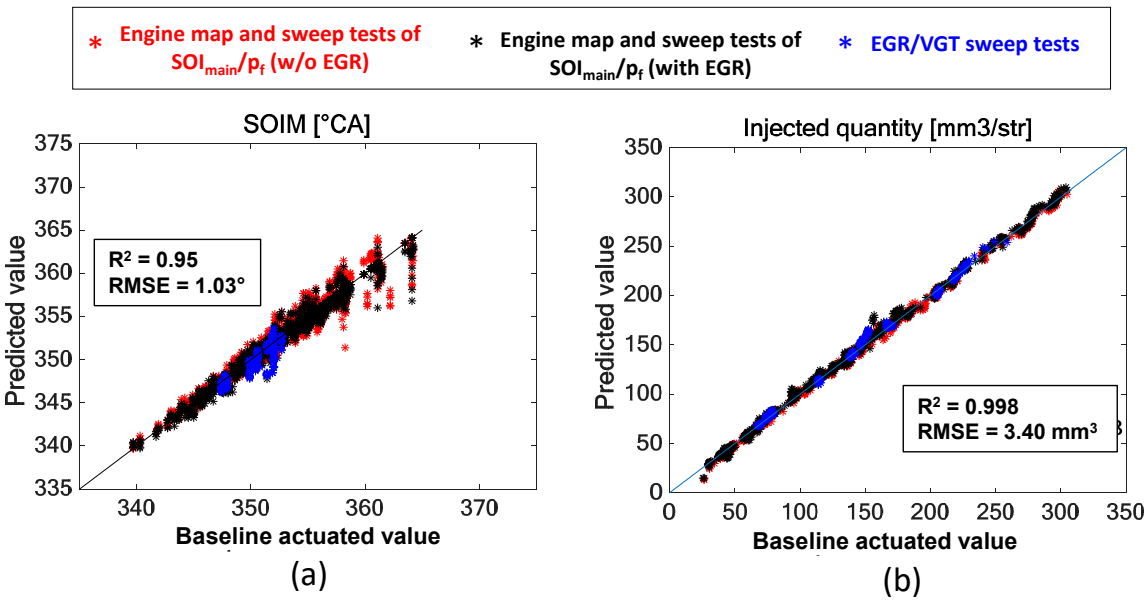

Figure 14. Model-based controller: calculated vs. actuated values of SOI_{main} (**a**) and $q_{f,inj}$ (**b**) for the steady-state conditions. The experimental values of IMEP and NO_x emissions were set as targets of the controller.

It can be seen that the RMSE of SOI_{main} is of the order of 1 degree, while the RMSE of the injected fuel quantity is of the order of 3.4 mm^3/cyl/stroke.

An additional functionality test was carried out, in order to check its capability to respond to different targets of NO_x emissions, with respect to the baseline experimental levels, while maintaining nominal values of IMEP targets. The results of this analysis are reported in Figure 15, which reports the values of SOI_{main} estimated by the controller vs. the baseline actuated values, when setting NO_x emissions targets equal to −40% (Figure 15a) and +40% (Figure 15b) with respect to the baseline experimental levels.

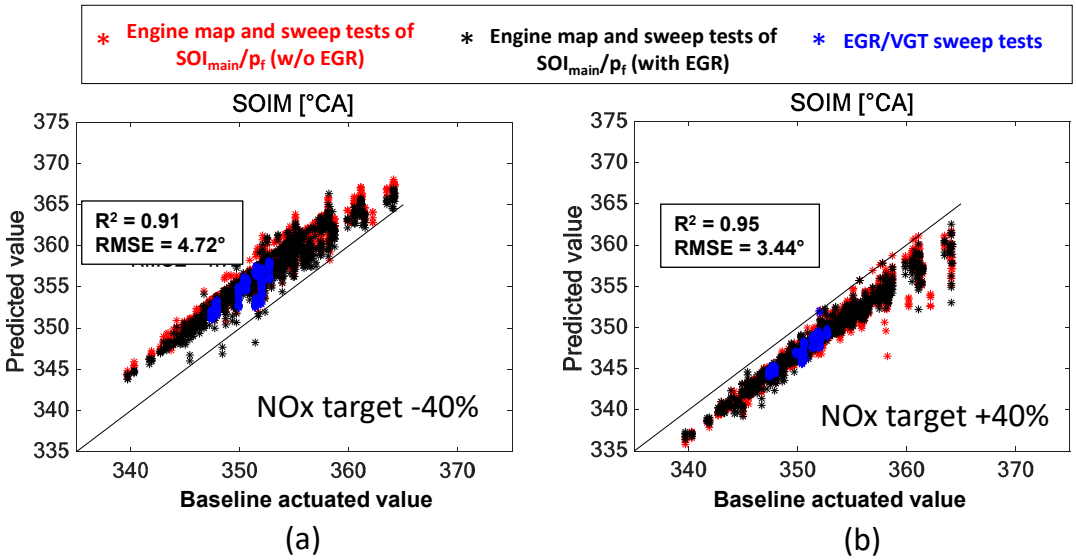

Figure 15. SOI_{main} values estimated by the controller vs. the baseline actuated values, when setting NOx emissions targets equal to −40% (**a**) and +40% (**b**) with respect to the baseline experimental levels.

It can be seen that the controller responds adequately to different NO_x target requests, by adjusting SOI_{main} in advance or in delay with respect to the nominal values actuated by the ECU.

Finally, another useful piece of information is related to the number of iterations which is required to achieve convergence, since it is strictly correlated to the overall computational time required by the controller. This information is shown in Figure 16, which reports the percentage of points which requires, for convergence, a lower or equal number of iterations than those reported in the *x*-axis, for the three different NO_x targets.

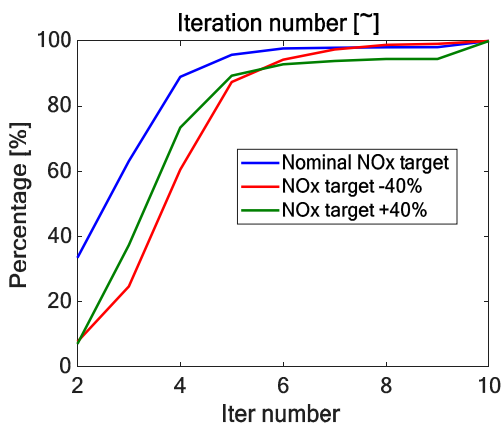

Figure 16. Model-based controller: percentage of points which requires, for convergence, a lower or equal number of iterations than those reported in the *x*-axis. The maximum number of allowed iterations was set at 10.

It can be seen that more than 90% of points requires a number of iterations which is lower or equal to 6. Therefore, when implemented on the real-engine, a maximum number of iterations equal to 6–8 can be set for the controller, which leads to an overall required computational time that is of the order of 2–3 ms.

7. Conclusions

A control-oriented real-time combustion model was assessed and applied to simulate BMEP (Brake Mean Effective Pressure) and NO_x (Nitrogen Oxide) emissions in an 11.0 L FPT Cursor 11 diesel engine for heavy-duty applications. The activity was carried out in the frame of the IMPERIUM (IMplementation of Powertrain Control for Economic and Clean Real driving emIssion and fuel ConsUMption") H2020 EU Project. The model was used to derive a model-based controller, which identifies the values of injected quantity and main injection timing in order to achieve the desired targets of indicated mean effective pressure and NO_x emissions.

First, the model was calibrated and assessed at steady-state conditions, considering engine map tests and sweep tests of injection timing and injection pressure, with and without EGR employment, as well as sweep-tests of VGT rack position and EGR. Within this analysis, several cases were considered, in which the input model parameters were obtained from accurate bench sensors or directly from the engine sensors. Subsequently, it was validated in transient operation over several load ramps at different engine speeds. In addition to BMEP and NOx emissions, additional combustion metrics were also included in the analysis, such as MFB50, peak firing pressure (PFP) and IMEP.

It was found that, at steady-state operation, the average error is of the order of 0.28–0.32 bar with reference to BMEP prediction, and of the order of 80–110 ppm with reference to NOx simulation, where the largest error occurs when ECU-derived input parameters are used. Similar accuracy levels were obtained in transient operation.

Subsequently, a statistical model robustness analysis was carried out, in order to verify the impact of the uncertainty in the input variables on the accuracy of the predicted quantities. It was found that the maximum values of RMSE are of the order of 1.4 bar for BMEP and 250 ppm for the NO_x emissions, in the worst cases. The main variable which affects the BMEP estimation accuracy is the injected fuel quantity, while the main variables which affect the NO_x emission estimation accuracy are the air and EGR mass. Therefore, an effort should be made in order to increase the accuracy of the injectors in realizing the desired fuel quantity and the accuracy of the sub-models that estimate the air and EGR mass, in order to increase the robustness of the proposed model. With reference to the NO_x simulation, it could also be beneficial to install an intake O_2 sensor in the engine in order to improve the model accuracy especially in transient operation, and when EGR is adopted.

A calibration sensitivity analysis was also carried out, in order to verify how the model accuracy is affected by a reduction of the points used for calibration. It was found that the accuracy of the model is virtually unaffected by the reduction of calibration points, even when the original calibration dataset is reduced by 80%.

It was verified that the proposed model features real-time capability, since the required computational time on the ETAS ES910 rapid prototyping device is of the order of 300–400 μs. Finally, the basic functionality of the model-based combustion controller was tested at steady-state conditions.

Author Contributions: The authors equally contributed to the deployment of the paper. Conceptualization, R.F., O.M., E.S.; Methodology, R.F., O.M.; Software, O.M.; Formal Analysis, R.F., O.M; Data Curation, R.F., O.M., A.M. (Alessandro Mancarella); Writing—Original Draft Preparation, R.F., O.M.; Writing—Review and Editing, R.F., O.M., G.H.; Supervision, A.M. (Antonio Mittica), E.S.; Resources; G.H.

Acknowledgments: The research leading to these results received funding from the European Union's Horizon 2020 research and innovation programme under grant agreement n° 713783 (IMPERIUM) and from the Swiss State Secretariat for Education, Research and Innovation (SERI) under contract n°16.0063 for the Swiss consortium members.

Conflicts of Interest: The authors declare no conflict of interest.

Abbreviations

AF	air-to-fuel ratio
AF_{st}	stoichiometric air-to-fuel ratio
ANN	artificial neural network
ATS	after-treatment system
BMEP	Brake Mean Effective Pressure (bar)
CA	crank angle (degree)
CFD	Computer Fluid-Dynamics
CLD	Chemiluminescence device
CNG	Compressed Natural Gas
CUC	Clean-Up Catalyst
DOC	Diesel Oxidation Catalyst
DPF	Diesel Particulate Filter
DT	dwell-time
ECU	Engine Control Unit
EGR	Exhaust Gas Recirculation
EOI	end of injection (degree)
EVO	Exhaust Valve Opening
FMEP	Friction Mean Effective Pressure (bar)
FPT	Fiat Powertrain Technologies
HCCI	Homogeneous Charge Compression Ignition
H_L	lower heating value of the fuel
ICE	Internal Combustion Engines
$IMEP_g$	gross Indicated Mean Effective Pressure (bar)
$IMEP_n$	net Indicated Mean Effective Pressure (bar)
IVC	Intake Valve Closing
K	combustion rate coefficient
m	mass
m_{air}	trapped air mass
m_{EGR}	trapped EGR mass
$m_{f,inj}$	total injected fuel mass (mg per cycle/cylinder)
$\dot{m}_{f,inj}$	fuel injection rate
MFB50	crank angle at which 50% of the fuel mass fraction has burned (degree)
n	polytropic coefficient for the compression phase
n'	polytropic coefficient for the expansion phase
N	engine rotational speed (1/min)
NEDC	New European Driving Cycle
O_2	intake charge oxygen concentration (%)
p	pressure (bar)
PCCI	Premixed Charge Compression Ignition
p_{EMF}	exhaust manifold pressure (bar abs)
p_f	injection pressure (bar)
PFP	peak firing pressure
p_{IMF}	intake manifold pressure (bar abs)
PMEP	Pumping Mean Effective Pressure (bar)
POD	Paramagnetic Oxygen Detector
q	injected fuel volume quantity (mm^3)
Q_{ch}	chemical heat release
$Q_{f,evap}$	fuel evaporation heat
$q_{f,inj}$	total injected fuel volume quantity per cycle/cylinder

Q_{fuel}	chemical energy associated with the injected fuel
$Q_{ht,glob}$	global heat transfer of the charge with the walls
Q_{net}	net heat release
R^2	squared correlation coefficient
RAF	Relative Air-to-Fuel ratio
Rh_{amb}	ambient relative humidity
RMSE	root mean square error
SOC	start of combustion
SCR	Selective Catalytic Reduction
SOI	electric start of injection
SOI_{main}	electric start of injection of the main pulse
SVM	support vector machine
t	time
T	temperature (K)
T_{amb}	ambient temperature
T_{EMF}	exhaust manifold temperature
T_{IMF}	intake manifold temperature
u^2	variance
V	volume
V2I	Vehicle-to-Infrastructure
V2V	Vehicle-to-Vehicle
V2X	vehicle-to-everything technology
VGT	Variable Geometry Turbine
VPM	Virtual Pressure Model
WLTP	Worldwide harmonized Light-duty Test Procedure
$X_{r,EGR}$	EGR rate
Greek symbols	
ρ	density
ρ_{SOI}	in-chamber ambient density evaluated at the SOI instant
σ	standard deviation
τ	ignition delay coefficient

References

1. Xue, X.; Rutledge, J. *Potentials of Electrical Assist and Variable Geometry Turbocharging System for Heavy-Duty Diesel Engine Downsizing*; SAE Technical Paper 2017-01-1035; SAE International: Warrendale, PA, USA, 2017.
2. Di Iorio, S.; Beatrice, C.; Guido, C.; Napolitano, P.; Vassallo, A.; Ciaravino, C. *Impact of Biodiesel on Particle Emissions and DPF Regeneration Management in a Euro5 Automotive Diesel Engine*; SAE Technical Paper 2012-01-0839; SAE International: Warrendale, PA, USA, 2012.
3. D'Ambrosio, S.; Gaia, F.; Iemmolo, D.; Mancarella, A.; Salamone, N.; Vitolo, R.; Hardy, G. *Performance and Emission Comparison between a Conventional Euro VI Diesel Engine and an Optimized PCCI Version and Effect of EGR Cooler Fouling on PCCI Combustion*; SAE Technical Paper 2018-01-0221; SAE International: Warrendale, PA, USA, 2018.
4. Ferrari, A.; Mittica, A.; Pizzo, P.; Jin, Z. PID Controller Modelling and Optimization in Cr Systems with Standard and Reduced Accumulators. *Int. J. Automot. Technol.* **2018**, *19*, 771–781. [CrossRef]
5. Ferrari, A.; Mittica, A.; Pizzo, P.; Wu, X.; Zhou, H. New methodology for the identification of the leakage paths and guidelines for the design of common rail injectors with reduced leakage. *J. Eng. Gas Turbines Power* **2018**, *140*, 022801. [CrossRef]
6. Finesso, R.; Marello, O.; Misul, D.; Spessa, E.; Violante, M.; Yang, Y.; Hardy, G.; Maier, C. Development and Assessment of Pressure-Based and Model-Based Techniques for the MFB50 Control of a Euro VI 3.0L Diesel Engine. *SAE Int. J. Engines* **2017**, *10*, 1538–1555. [CrossRef]
7. Finesso, R.; Hardy, G.; Marello, O.; Spessa, E.; Yang, Y. Model-Based Control of BMEP and NOx Emissions in a Euro VI 3.0L Diesel Engine. *SAE Int. J. Engines* **2017**, *10*. [CrossRef]

8. Finesso, R.; Spessa, E.; Yang, Y.; Conte, G.; Merlino, G. *Neural-Network Based Approach for Real-Time Control of BMEP and MFB50 in a Euro 6 Diesel Engine*; SAE Technical Paper 2017-24-0068; SAE International: Warrendale, PA, USA, 2017.
9. Giakoumis, E.G. Diesel and Spark Ignition Engines Emissions and After-Treatment Control: Research and Advancements. *Energies* **2017**, *10*, 1882. [CrossRef]
10. Yamaguchi, T.; Aoyagi, Y.; Uchida, N.; Fukunaga, A.; Kobayashi, M.; Adachi, T.; Hashimoto, M. Fundamental Study of Waste Heat Recovery in the High Boosted 6-cylinder Heavy Duty Diesel Engine. *SAE Int. J. Mater. Manf.* **2015**, *8*, 209–226. [CrossRef]
11. Delogu, M.; Zanchi, L.; Dattilo, C.; Maltese, S.; Riccomagno, R.; Pierini, M. *Take-Home Messages from the Applications of Life Cycle Assessment on Lightweight Automotive Components*; SAE Technical Paper 2018-37-0029; SAE International: Warrendale, PA, USA, 2018.
12. Finesso, R.; Misul, D.; Spessa, E.; Venditti, M. Optimal Design of Power-Split HEVs Based on Total Cost of Ownership and CO2 Emission Minimization. *Energies* **2018**, *11*, 1705. [CrossRef]
13. Talavera, E.; Díaz-Álvarez, A.; Jiménez, F.; Naranjo, J.E. Impact on Congestion and Fuel Consumption of a Cooperative Adaptive Cruise Control System with Lane-Level Position Estimation. *Energies* **2018**, *11*, 194. [CrossRef]
14. Breakthrough: New Bosch Diesel Technology Provides Solution to NOx Problem. Available online: https://www.bosch-presse.de/pressportal/de/en/breakthrough-new-bosch-diesel-technology-provides-solution-to-nox-problem-155524.html/ (accessed on 12 October 2018).
15. IMPERIUM Project Information. Available online: http://www.imperium-project.eu/project-information/ (accessed on 12 October 2018).
16. Rakopoulos, C.; Giakoumis, E. *Review of Thermodynamic Diesel Engine Simulations under Transient Operating Conditions*; SAE Technical Paper 2006-01-0884; SAE International: Warrendale, PA, USA, 2006.
17. Finesso, R.; Spessa, E.; Yang, Y. Development and Validation of a Real-Time Model for the Simulation of the Heat Release Rate, In-Cylinder Pressure and Pollutant Emissions in Diesel Engines. *SAE Int. J. Engines* **2016**, *9*, 322–341. [CrossRef]
18. Asprion, J.; Chinellato, O.; Guzzella, L. A fast and accurate physics-based model for the NOx emissions of Diesel engines. *Appl. Energy* **2013**, *103*, 221–233. [CrossRef]
19. Asprion, J.; Chinellato, O.; Guzzella, L. Optimisation-oriented modelling of the NOx emissions of a Diesel engine. *Energy Convers. Manag.* **2013**, *75*, 61–73. [CrossRef]
20. Andersson, M.; Johansson, B.; Hultqvist, A.; Noehre, C. *A Predictive Real Time NOx Model for Conventional and Partially Premixed Diesel Combustion*; SAE Technical Paper 2006-01-3329; SAE International: Warrendale, PA, USA, 2006.
21. Najafi, B.; Faizollahzadeh Ardabili, S.; Mosavi, A.; Shamshirband, S.; Rabczuk, T. An Intelligent Artificial Neural Network-Response Surface Methodology Method for Accessing the Optimum Biodiesel and Diesel Fuel Blending Conditions in a Diesel Engine from the Viewpoint of Exergy and Energy Analysis. *Energies* **2018**, *11*, 860. [CrossRef]
22. Brusca, S.; Lanzafame, R.; Messina, M. *A Combustion Model for ICE by Means of Neural Network*; SAE Technical Paper 2005-01-2110; SAE International: Warrendale, PA, USA, 2005.
23. Bennett, C.; Dunne, J.F.; Trimby, S.; Richardson, D. Engine cylinder pressure reconstruction using crank kinematics and recurrently-trained neural networks. *Mech. Syst. Signal Process.* **2016**, *85*, 126–145. [CrossRef]
24. Li, H.; Butts, K.; Zaseck, K.; Liao-McPherson, D.; Kolmanovski, I. *Emissions Modeling of a Light-Duty Diesel Engine for Model-Based Control Design Using Multi-Layer Perceptron Neural Networks*; SAE Technical Paper 2017-01-0601; SAE International: Warrendale, PA, USA, 2017.
25. Johri, R.; Salvi, A.; Filipi, Z. Real-time Transient Soot and NOx Virtual Sensors for Diesel Engine Using Neuro-Fuzzy Model Tree and Orthogonal Least Squares. *J. Eng. Gas Turbines Power* **2012**, *134*, 092806. [CrossRef]
26. Finesso, R.; Hardy, G.; Maino, C.; Marello, O.; Spessa, E. A New Control-Oriented Semi-Empirical Approach to Predict Engine-Out NOx Emissions in a Euro VI 3.0 L Diesel Engine. *Energies* **2017**, *10*, 1978. [CrossRef]
27. Heywood, J.B. *Internal Combustion Engine Fundamentals*; McGraw-Hill Intern: Columbus, OH, USA, 1988.

28. Small Engine and Powered Equipment Committee. *Test Procedure for the Measurement of Gaseous Exhaust Emissions from Small Utility Engines*; SAE J1088_201303 Recommended Practice; SAE International: Warrendale, PA, USA, 2013.
29. Catania, A.; Finesso, R.; Spessa, E. *Real-Time Calculation of EGR Rate and Intake Charge Oxygen Concentration for Misfire Detection in Diesel Engines*; SAE Technical Paper 2011-24-0149; SAE International: Warrendale, PA, USA, 2011.

© 2019 by the authors. Licensee MDPI, Basel, Switzerland. This article is an open access article distributed under the terms and conditions of the Creative Commons Attribution (CC BY) license (http://creativecommons.org/licenses/by/4.0/).